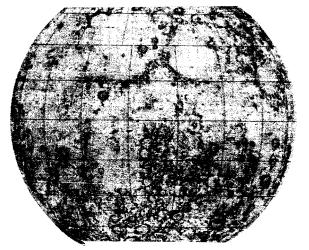
ASTROGEOLOGIC STUDIES

ANNUAL PROGRESS REPORT

August 25, 1962 to July 1, 1963

Norm 80%	66	35596	N 6
	- (ACCESSION NUMBER)		• 3
, T.Y		(PAGES)	
FAGIL	CK.	5862	
	INASA CR	OR TMX OR AD NUMBER)	_



PART D
STUDIES FOR SPACE FLIGHT PROGRAM

GPO PRICE \$ _____



Hard copy (HC)

ff 653 July 65

DEPARTMENT OF THE INTERIOR

UNITED STATES GEOLOGICAL SURVEY

REPORTS CONTROL No.

ASTROGEOLOGIC STUDIES ANNUAL PROGRESS REPORT

August 25, 1962 to July 1, 1963

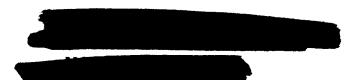
PART D: STUDIES FOR SPACE FLIGHT PROGRAM

May 1964

This preliminary report is distributed without editorial and technical review for conformity with official standards and nomenclature. It should not be quoted without permission.

This report concerns work done on behalf of the National Aeronautics and Space Administration.

DEPARTMENT OF THE INTERIOR
UNITED STATES GEOLOGICAL SURVEY



CONTENTS

	Page
PART DSTUDIES FOR SPACE FLIGHT PROGRAM	
Introduction	x
1. A photometric technique for measurement of lunar slopes,	
by D. E. Wilhelms	1
Introduction	1
Assumptions and basis of the technique	1
Procedure	3
Automation	10
Results to date	11
Reference	12
2. A lunar isotonal map, by Robert J. Hackman	13
Introduction	13
Procedure	18
Interpretations and conclusions	26
References	28
3. Lunar infrared emission study, by Kenneth Watson	29
References	33a
4. Density of small craters on the lunar surface, by	
H. J. Moore	34
Introduction	34
Mass and number of bodies impacting the lunar	
surface	34
Density of secondary-impact craters	44
Conclusions	49
References	50

CONTENTS--Continued

4		Page
7 5.	Change in effective target strength with increasing size	
	of hypervelocity impact craters, by H. J. Moore, D. E.	
	Gault, and E. D. Heitowit	52
	Introduction	52
	Experimental conditions and results	53
	Target strength	57
	Change of strength with size	58
	Explanation of experimental results	59
	Conclusions	61
/	References	61
V 6.	Photogrammetric mapping of experimental craters, by	
	R. V. Lugn	64
	Introduction	64
	Procedure	66
	References	70
V7.	Photographic and photoelectric investigations of the	
	Earth-Moon libration regions L_4 and L_5 from Mt.	
	Chacaltaya, Bolivia, by E. C. Morris, J. Ring, and	
	H. G. Stephens	71
	References	74
√ 8.	Semi-micro X-ray fluorescence analysis of tektites	
	using 50 milligram samples, by H. J. Rose, Jr.,	
	F. Cuttitta, M. K. Carron, and R. Brown	75

CONTENTS--Continued

		Page
	Introduction	75
	X-ray fluorescence method	77
	Chemical analytical methods	78
	References	82
9.	Computer analysis of areal microphotometer data	
	from lunar photographs, by A. T. Miesch and	
	C. W. Davis	85
	Procellarian mare material	95
	Apenninian regional material	107
	Conclusions	109
	References	114

ILLUSTRATIONS

	Page
PART D, STUDIES FOR SPACE FLIGHT PROGRAM	
1. A photometric technique for measurement of lunar slopes.	
Figure 1.1 Principle of photometric slope determination	- 2
1.2 Example of microphotometer trace and corresponding	
comparison curve in lunar surface material of	
uniform albedo (from traverse north of Ptolemaeus	•
in Imbrian sculpture terrain overlain by	
Apenninian regional material)	- 4
1.3 Slope frequency distribution curve for Apennine	
Mountains between 14°N. and 17°N., 570 slopes	
each .75 km long	7
1.4 Slope frequency distribution curve for mare	
material, 193 segments of 1.5 km each in Oceanus	
Procellarum and Sinus Medii	- 8
1.5 Hypothetical microphotometer trace of flat surface	
consisting of materials of three different	
albedos	- 9
2. A lunar isotonal map.	
Figure 2.1 Index map showing location of the Lansberg region o	f
the Moon	- 14
2.2 A high-contrast enlargement of a full-moon photogra	ph
of the Lansberg region of the Moon. XY is locati	on
of traverse for density curves shown in figure 3.	

ILLUSTRATIONS -- Continued

		Page
	A is brightest point. B is darkest point.	
	C, D, E, and F (maria) all have the same tone	
	value. G is small dark area of the same tone	
	value as H. Ray at I has same tone value as	
	maria at J	15
2.3	Densitometer curves for traverse across Lansberg	
	region on (A) high-contrast film, (B) medium-	
	contrast and (C) low-contrast	17
2.4	Densitometer and recorder: (A) stable base film	
	transparency; (B) stable base print for recording	
	location of traverse; and (C) curve showing photo-	
	graphic density along traverse	19
2.5	Diagram shows relationship of density curve to	
	stepped curve of density wedge. Curve AB shown in	
	figure 6 at larger scale	20
2.6	Enlargement of part of curve shown in figure 5.	
	Density values determined from curve are projected	
	to line AB for transfer to compilation photograph-	21
2.7	Isotonal map of the Lansberg region of the Moon show	,
	ing configuration of contours. Blocked out area	
	shown in figure 8 at larger scale	23
2.8	Part of isotonal map of the Lansberg region super-	
	imposed on the U.S. Air Force chart	24

ILLUSTRATIONS -- Continued

	Page
2.9 Comparison of 29 normal albedo measurements	
with tone measurements made on the high-	
contrast film positive of the Lansberg region	25
4. Density of small craters on the lumar surface.	
Figure 4.1 Cumulative frequency of impacts of bodies of mass	
m with the surface of the Moon	36
4.2 Predictions of area occupied by craters	43
5. Change of effective target strength with increasing size of	
hypervelocity impact craters.	
Figure 5.1 Experimental relationship between ejected mass and	
projectile properties	55
6. Photogrammetric mapping of experimental craters.	
Figure 6.1 Stereoscopic pair of photographs of an experimental	
crater in basalt	65
6.2 Topographic and structural map of hypervelocity	
impact crater in basalt	69
9. Computer analysis of areal microphotometer data from	
lunar photographs.	
Figure 9.1 Index map showing location of area of study (Ar, Ap-	
enplaian regional material; Pm, Procellarian mare	
materia1)	86
9.2 Generalized flow chart for computer program being	
prepared to analyze microphotometer data (Davis	
and others, 1963)	93

ILLUSTRATIONS--Continued

		Page
9.3	Autocorrelation curves computed from original data	
	(order of trend = 0) and deviations from trends	
	of order 1 to 5 (Apenninian regional material)	
	and 1 to 4 (Procellarian mare material)	94
9.4	Method of lagging areal data for construction of	
	serial correlation surfaces	96
9.5	Component parts of the serial correlation surface-	97
9.6	Histograms of microphotometer measurements:	
	Procellarian mare material	98
9.7	Contour map of original microphotometer measurements:	
	Procellarian mare material	101
9.8	Contour map of first order and second order poly-	
	nomial surfaces (trends) fitted to microphotometer	
	data in figure 5.7: Procellarian mare material-	102
9.9	Contour map of deviations of original microphotometer	
	measurements from fitted second order trend:	
	Procellarian mare material	103
9.10	Contour map of serial correlation surface:	
	Procellarian mare material	105
9.11	Autocorrelation curves for Procellarian mare	
	material	106

ILLUSTRATIONS--Continued

		Page
9.12	Histogram of microphotometer measurements:	
	Apenninian regional material	108
9.13	Contour map of original microphotometer measure-	
	ments: Apenninian regional material	110
9.14	Contour map of first order and second order poly-	
	nomial surfaces (trends) fitted to microphotometer	
	data in figure 9.13: Apenninian regional	
	material	111
9.15	Contour map of deviations of original microphotometer	
	measurements from fitted second order trend:	
	Apenninian regional material:	112
9.16	Contour map of serial correlation surface:	
	Apenninian regional material	113

TABLES

	Page
PART D, STUDIES FOR SPACE FLIGHT PROGRAM	
8. Semi-micro x-ray fluorescence analysis of tektites	
using 50 milligram samples.	
Table 8.1 Summary of crystals, detectors and wavelengths	79
8.2 Comparison of x-ray and chemical analyses of	
6 Java tektites	80
9. Computer analysis of areal microphotometer data.	
Table 9.1 Procellarian mare material: Analysis of variance	
of polynomial regression surfaces	90
9.2 Apenninian regional material: Analysis of	
variance of polynomial regression surfaces	91

INTRODUCTION

This Annual Report is the fourth of a series describing the results of research conducted by the U. S. Geological Survey on behalf of the National Aeronautics and Space Administration. This report, which covers the period August 25, 1962 to July 1, 1963, is in four volumes corresponding to four main areas of research: Part A, Lunar and Planetary Investigations; Part B, Crater and Solid State Investigations; Part C, Cosmochemistry and Petrography; and Part D, Studies for Space Flight Program. An additional volume presents in abstract form summaries of the papers in Parts A, B, C, and D.

The major long-range objectives of the astrogeologic studies program are to determine and map the stratigraphy and structure of the Moon's crust, to work out from these the sequence of events that led to the present condition of the Moon's surface, and to determine the processes by which these events took place. Work being carried out that leads toward these objectives includes a program of lunar geologic mapping; studies on the discrimination of geologic materials on the lunar surface by their photometric, polarimetric, and infrared properties; field studies of structures of impact, explosive, and volcanic origin; laboratory studies on the behavior of rocks and minerals subjected to shock; study of the effect of stress history on the solid state properties of rocks; study of the chemical, petrographic and physical properties of materials of possible lunar origin and the development of techniques for their microanalysis and nondestructive analysis; and engineering studies in aid of the design of space flight experiments and the planning of space missions.

Part A: Lunar and Planetary Investigations (with map supplement), contains the preliminary results of detailed geologic mapping on a 1:1,000,000 scale of a major part of the equatorial belt of the Moon. Detailed geologic relations in certain areas and some regional geologic problems are discussed.

Part B: Crater Investigations, includes a study of a naturally occurring analogue of a secondary cratering event; a report on the progress of shock equation of state studies; reports on the high pressure polymorphs of silica, stishovite and coesite; and preliminary reports on field investigations conducted on meteorite craters of Campo del Cielo, Argentina, and the crypto-explosion structure of Flynn Creek, Tennessee.

Part C: Cosmochemistry and Petrography, includes reports on the chemistry of tektites, their behavior during heating, the nature of the magnetic spherules visible in some tektites and evidence for their presence in submicroscopic sizes in others. Reports on metallic iron and copper in stony meteorites are also included.

Part D: Studies for Space Flight Program, includes reports on the determination of lunar slopes by photometric methods; a method for outlining isotonal areas on the lunar surface; a derivation of the expected frequency of small craters on the lunar surface; and a report on the change of effective strength of target materials with crater size.

Reports on a search for matter in the Earth-Moon libration regions, infrared studies, x-ray fluorescence of tektites, photogrammetry of small craters, and computer analysis of the pattern of varying albedo over the lunar terrain are also included.

A PHOTOMETRIC TECHNIQUE FOR MEASUREMENT

OF LUNAR SLOPES

by D. E. Wilhelms

Introduction

A technique is being developed for determination of lunar slopes on the basis of darkening by shadows using a single photograph. The present paper is a preliminary outline of the method; more complete accounts will appear as work progresses. The principle underlying the technique was first stated by van Diggelen (1951), and applied by him to low mare ridges. His final product was profiles and contour maps of single ridges. The present writer is extending the technique to all types of terrain, greatly expanding the amount of data produced by systematic methods, and expressing the results in terms of slope frequency distribution curves and maps of wide areas of the lunar terrain. The technique developed largely during discussions with E. M. Shoemaker, who suggested the general approach, and R. E. Eggleton;

Assumptions and basis of the technique

the writer is indebted to them for their help.

The technique rests upon the assumption that, for slopes on lunar surface material of uniform albedo, the apparent brightness depends only on the angle of incidence of the sun's rays. In figure 1.1, the slope of a portion of the lunar surface (P) is equal to the

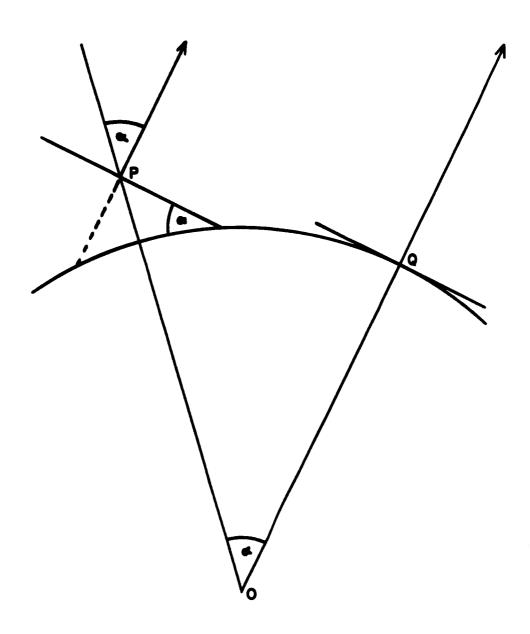


Figure 1.1. Principle of photometric slope determination.

angular distance (α) measured in a direction normal to the terminator, from a horizontal portion of the surface (Q) with the same brightness. It is immaterial what features of the microrelief, superimposed on the macrorelief, actually produce the shadows which combine to produce darkening. East-west components of slope are obtained. Completely black cast shadows cannot be treated by the technique. To date the effect of reflection of light from surrounding terrain into shadowed regions has not been considered, but this will have to be done in more refined work.

Procedure

Negative photographs on glass are traversed with a microphotometer. Traverses are made parallel to lunar latitude lines, i.e., closely perpendicular to the terminator. On the best photographs so far employed, the longest traverses have extended to about 16 degrees of lunar longitude away from the terminator; beyond that, there is not enough darkening on most slopes to deflect the recorder sufficiently. The best results have been obtained in regions near the center of the Moon's disk. The microphotometer record is in two forms: an inked line on a chart, and a digitized punched paper tape. The technique was developed using the charts. A method of automating it by use of the tapes is being developed at present and is discussed below.

An example of the chart record is shown in figure 1.2. The microphotometer measures the amount of light transmitted by the photographic

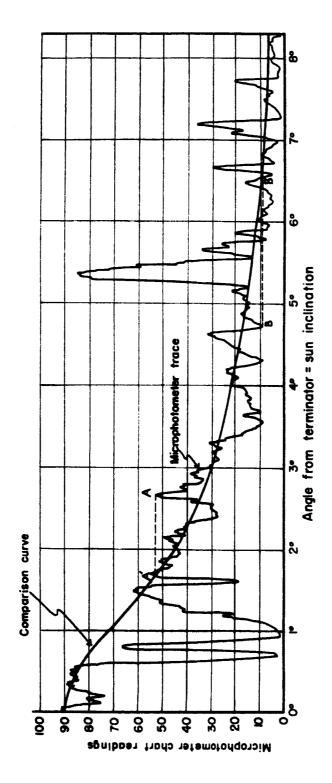


Figure 1.2. Example of microphotometer trace and corresponding (from traverse north of Ptolemaeus, in Imbrian sculpture tercomparison curve in lunar surface material of uniform albedo rain overlain by Apenninian regional material).

plate; high numbers represent high transmission. (The machine is adjusted so that 90 represents full transmission to avoid going over 100, which would be read as 0 by the digitizer.) Since negative plates are employed, light areas on the plates represent dark areas on the Moon, i.e., shadows and rocks of low albedo. The response of the microphotometer is logarithmic, so that light areas on the plates produce exaggerated upward deflections. This is the reason for using negatives: deflections representing shadows are stressed, while deflections representing variations in albedo of light rocks, meaningless to the problem at hand, are suppressed.

Basic to the technique is the establishment of a "comparison curve,"
i.e., the curve against which actual readings are compared (fig. 1.2).

It is the curve that would be obtained from microphotometer traverses

if the lunar surface were flat down to segments of 1 or 2 kilometers,

and if it consisted of rock of uniform albedo.

Actual rugged lunar topography yields a much more irregular curve. At any given distance from the terminator, a slope facing towards the terminator is darker (lighter on the negative) than a horizontal surface would be at the same point; its chart reading is therefore above the comparison curve. By drawing a horizontal line between the chart reading for the slope and the comparison curve (dotted line A-A' in fig. 1.2) the point on the comparison curve which has the same brightness is immediately located. Distance from the terminator for all points is scaled off on the chart, and since this distance is equal to the angle of incidence of the sun's rays, the length in degrees of the horizontal

line is a measure of the difference in angle of incidence at the two points. It is therefore a direct measure of the slope in question.

Similar reasoning applies to slopes which are brighter than horizontal surfaces at the same point would be. They give deflections which
dip below the comparison curve (because they are dark on the negative
plates). The values of the slopes are determined by drawing a horizontal line to the right until it intersects the comparison curve (B-B¹).

By this simple procedure the slope of a large number of points can be determined in a short time. To date, the practice has been to obtain the average slope (regardless of what the small segments of slope contributing to the average are) for every segment of 0.05 degrees of lunar longitude, corresponding to 1.5 kilometer at the equator. The data are plotted as cumulative slope frequency distribution curves (figs. 1.3 and 1.4).

The accuracy of the technique depends upon the accuracy with which the comparison curve is drawn. The best way of determining it is to note areas on the photograph along the traverse which appear to be horizontal and to mark the portions of the microphotometer trace which correspond to them. The comparison curve is then drawn through these portions, and the remaining segments are drawn by interpolation.

Until now it has been assumed that traverses pass over surface materials of uniform albedo. Of course, for long traverses this is seldom the case. A curve for the hypothetical case of a horizontal surface of diverse albedo is shown in figure 1.5. Dotted lines show the extrapolation of the individual portions into complete comparison curves, one

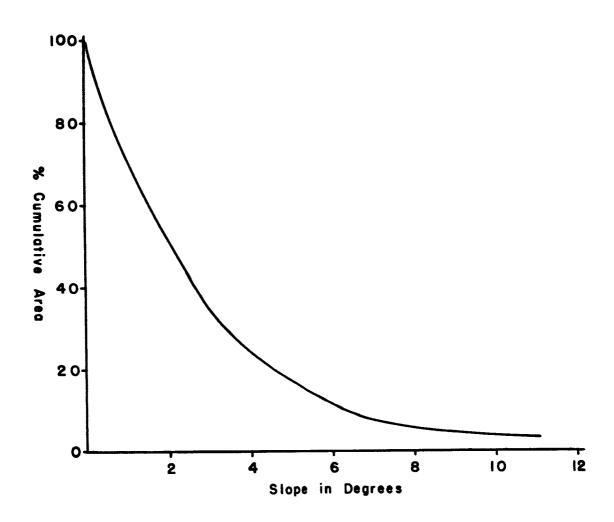


Figure 1.3. Slope frequency distribution curve for Apennine Mountains between $14^{\circ}N$ and $17^{\circ}N$, 570 slopes each .75 km long.

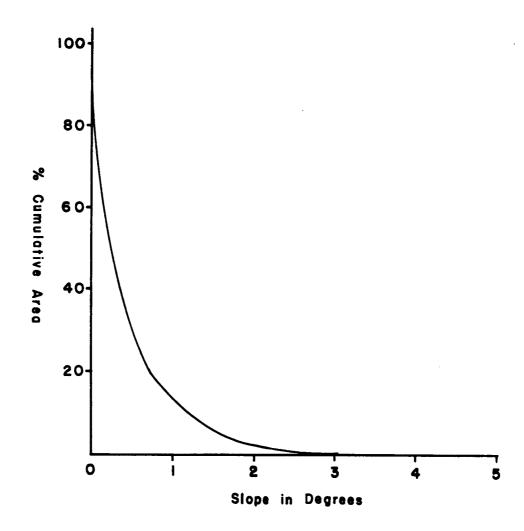


Figure 1.4. Slope frequency distribution curve for mare material, 193 segments of 1.5 km each in Oceanus Procellarum and Sinus Medii.

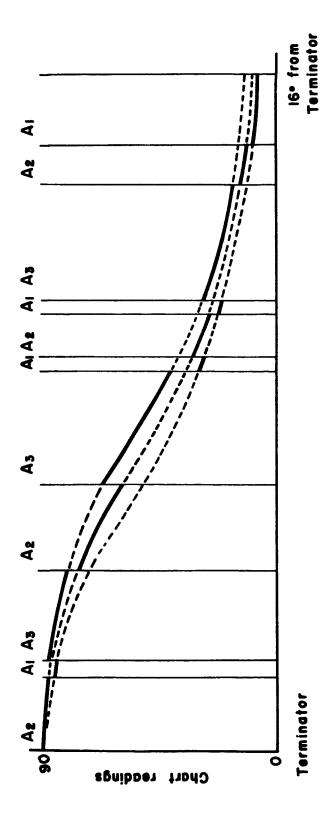


Figure 1.5. Hypothetical microphotometer trace of flat surface consisting of materials of three different albedos.

for each albedo unit. In most actual traverses the microphotometer traces are too complex to permit separation of the effects of albedo from the effects of shadows. Therefore, it is necessary to map in advance the regions of differding albedos, and to mark their contacts on the record chart. If this is done, comparison curves can be drawn in the manner described previously for the case of a single albedo unit. The best results will be obtained in areas mapped geologically, since the albedos for each geologic unit are (or soon will be) known.

Automation

The technique lends itself nicely to automation. In addition to the graph, a punched tape is produced during the traverses. The digits on it correspond to the chart readings of 00.0 to 90.0. The optimum running rate has proved to be that which produces one digit for every interval of the distance measured graphically, i.e., 0.05 degrees or 1.5 kilometers; the digitizer integrates for only half this distance, giving a sample size of .75 km. The digit is an average for this size segment, exactly what is desired. By adjusting the speed of the digitizer, a larger sample can be averaged, and when photographs of higher resolution than present ones become available, a smaller sample can be taken.

To date, the method of handling the comparison curve by the digit method has been to draw it graphically as described, and then to construct a table from it of the chart values corresponding to every

0.05 degrees of sun inclination. The digit for each bit of traverse is then simply located on the table, the corresponding sun inclination read off and the terminator distance of the traverse segment subtracted from it. The answer is either positive or negative; its absolute value is the value of the slope.

In the future, complete automation by computer should be possible as soon as a way is found to derive the comparison curves mathematically. Digits indicating albedo unit contacts will be entered on the tape and a separate comparison curve found for each. Once these are known, the remainder of the computations are very simple. Complete slope frequency distribution curves for geologic units and portions thereof should be able to be produced in the time it takes to run a traverse.

Results to date

Figures 1.3 and 1.4 are examples of slope frequency distribution curves thus far obtained. Figure 1.3 is from a rugged portion of the Apennine Mountains overlain by the regional Apennine ejecta blanket. The other, showing far less relief, is from a portion of the maria. Other curves of somewhat less reliability owing to variations in albedo have been obtained. In the near future many more curves, representing geologic units and portions of units, will be obtained. Terrain maps, on which areas of equal slope are delimited, will be constructed. This information is of great importance in constructing a model of the lunar surface for use in planning spacecraft landings.

Reference

Diggelen, J. van, 1951, A photometric investigation of the slopes and heights of the ranges of hills in the maria of the Moon: Astron.

Inst. Netherlands Bull., v. 11, p. 283-289.



A LUNAR ISOTONAL MAP

by Robert J. Hackman

Introduction

N 66 35598

The lunar maria, where not covered with ray material, generally display subtle differences in brightness, which may be related to local differences in texture and composition. Theoretically, the most precise way of investigating these differences is to measure normal albedo (absolute brightness) at individual points on the lunar surface. A few such measurements have been made, more on bright areas than on the dark maria. To be useful in geologic mapping, albedo measurements would have to be made at a great number of points covering the surface of the Moon; the technical difficulty of the measurements precludes this.

Tone values obtained by measurement of density of photographs provide a less precise measure of brightness than do telescopic measurements of normal albedo. On the other hand, photographic measurements of relative density can be made at all points on a lunar photograph independent of changes in atmospheric transmission or solar illumination. In this study an isotonal map was prepared by outlining areas of equal density on a photograph.

The Lansberg region of the Moon (figures 2.1 and 2,2) is located in the center of the western half of the lunar disk. It covers forty degrees of latitude and thirty degrees of longitude, and includes an

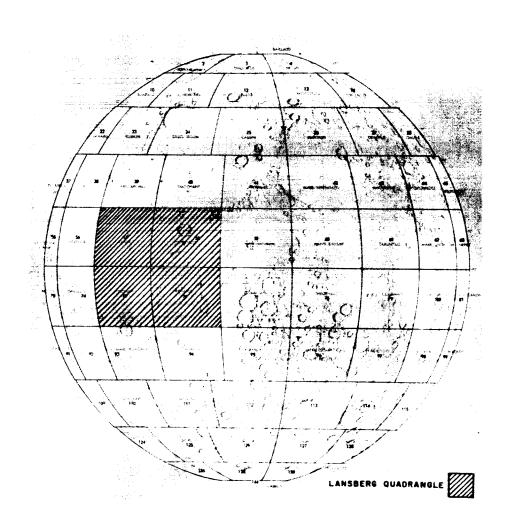
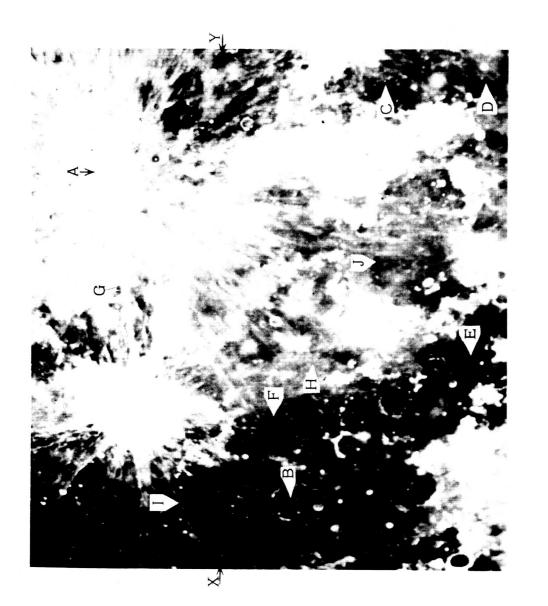


Figure 2.1. Index map showing location of the Lansberg region of the moon.



darkest point. C, D, E, and F (maria) all have the same tone value. of the Lansberg region of the Moon. XY is location of traverse for density curves shown in figure 2.3 A is brightest point. B is Figure 2.2. A high contrast enlargement of a full-moon photograph G is small dark area of the same tone value as H. Ray at I has same tone value as maria at J.

area of about 400,000 square miles. A full-moon photograph in which no shadows are present (figure 2.2), was chosen for the density measurements.

Densitometer traverses were made across high, medium and low-contrast full-moon positive transparencies to determine the most suitable contrast for enhancement of the darker tone values on the maria. The transparencies (1:8,000,000 scale) were printed on Eastman Kodak masking film from a glass plate negative (1:20,000,000 scale). The different contrasts were produced by varying the exposure time during the printing process.

Figure 23 shows the densitometer curves for the three traverses across the Lansberg region of the Moon. The location of the traverse line is shown as XY in figure 2.2. The curves demonstrate that the high-contrast film was exposed so as to enhance tone contrast in the darker parts of the photographs (the maria). As a consequence, tone differences in the brighter parts of the photograph (highlands and rays) are diminished. The dark tones are shifted from the shoulder of the gamma curve to the straight line portion and exhibit more contrast. The brighter tones are shifted to the toe of the curve and exhibit less contrast. A similar high-contrast film transparency from the same negative but at a larger scale was selected for the study.

^{1/} Mt. Wilson Observatory photograph, H. Wright series, no. 198, July 11, 1938.

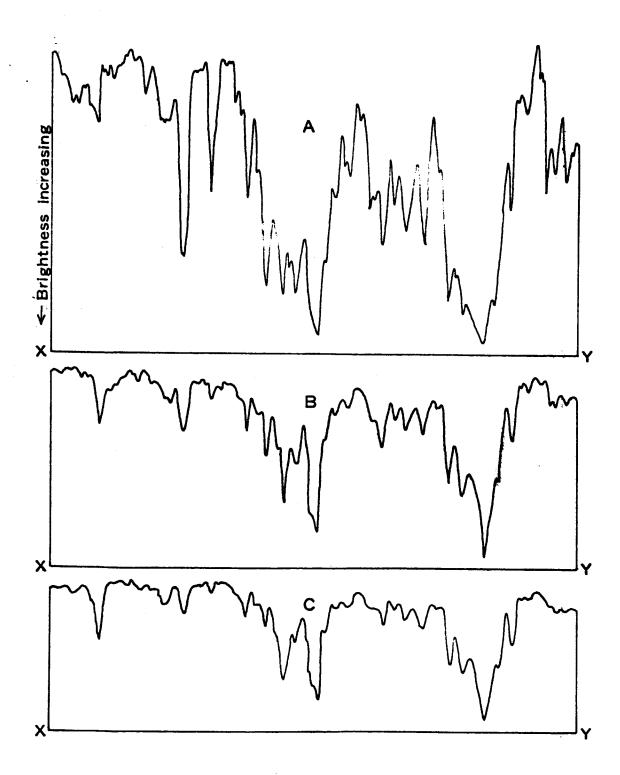


Figure 2.3. Densitometer curves for traverse across Lansberg region on (A) high-contrast film, (B) medium-contrast film and (C) low-contrast film.

Procedure

Film density was measured with a MacBeth Ansco densitometer, using a circular aperture of one millimeter (see figure 2.4). A positive transparency at a scale of 1:4,250,000 is placed at position A on the densitometer, and a stable-base positive print (Dupont Cronopac) at the same scale is placed at B. The two photographs are secured to a power-driven movable stage, and all lines of traverse are followed across both. The densitometer curve for each traverse is simultaneously plotted on graph paper by the recorder at C.

A control traverse was run over a standard density wedge to provide a relative scale of density increments preceding and following a set of 32 traverses. Six hundred spot measurements of density were also made.

Figure 2.5 shows how each traverse curve was related to the stepped curve of the density wedge. With the stepped curve as a guide, parallel lines were drawn, separating the traverse curve into density units. An enlarged portion of the curve (figure 2.6) shows how values and widths of density units were projected and plotted on a line representing the traverse.

Traverse lines, point locations, and density values were projected from the transparency sato a high-contrast stable-base positive print (Dupont Cronopac) enlarged to 1:2,000,000. The graphic records determined from the density curves were enlarged to the same scale and plotted



Figure 2.4. Densitometer and recorder: (A) stable base film transparency; (B) stable base print for recording location of traverse; and (C) curve showing photographic density along traverse.

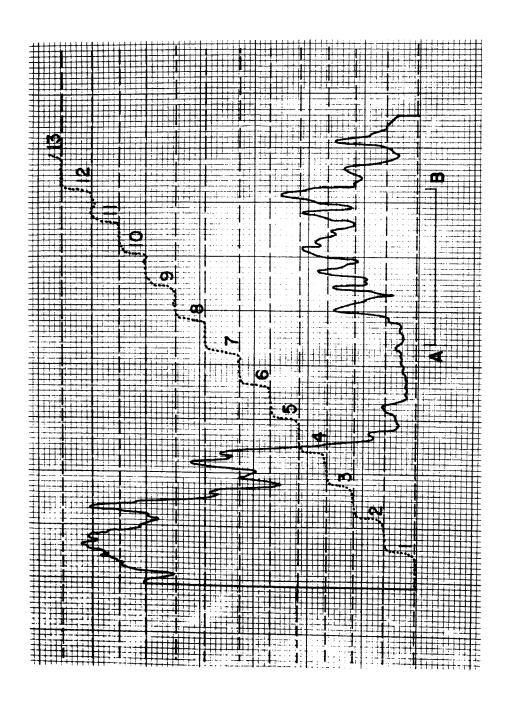


Figure 2.5. Diagram shows relationship of density curve to stepped Curve AB shown in figure 2.6 at larger curve of density wedge. scale.

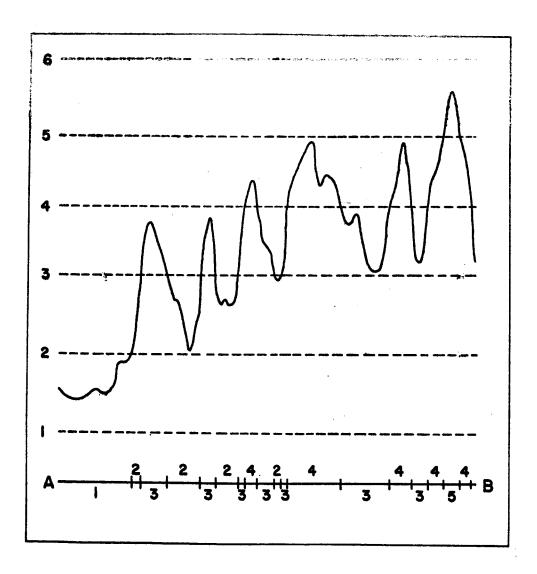


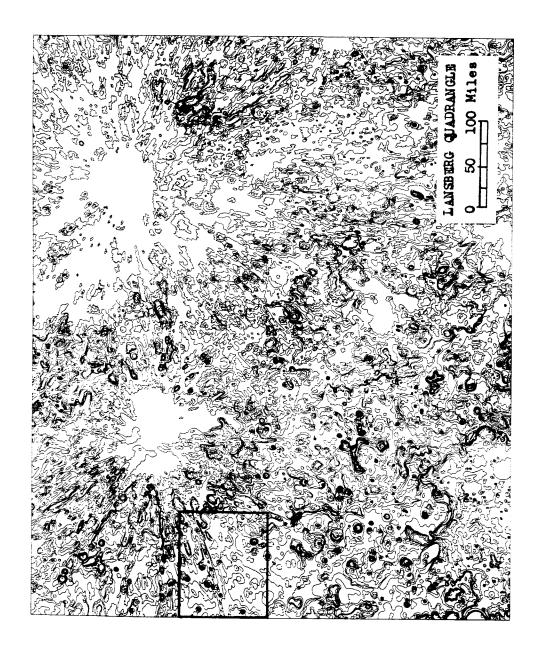
Figure 2.6. Enlargement of part of curve shown in figure 2.5. Density values determined from curve are projected to line AB for transfer to compilation photograph.

along their traverses. With the spot and traverse measurements as control, and tonal patterns on the photograph as visual aids for interpretation, isotonal lines connecting points of equal density were drawn on the photograph.

Coordinate intercepts of latitude and longitude (from Kuiper, 1961) along with recognizable features on the full-moon photograph, were used as control in transferring the isotonal lines to the Mercator projection of the U.S. Air Force lunar topographic chart. The transfer was done with a Zeiss-Agrotopograph Sketchmaster, modified with a supplemental lens providing gradational distortion in one direction only. Figure 2.7 shows the configuration of isotonal lines on the map; figure 2.8 shows a portion of the isotonal map (Hackman, 1963) superimposed on the Air Force topographic chart.

Isotonal lines delimiting certain features such as small bright craters on the lunar maria probably do not reflect properly the abrupt change associated with the margin of such features. This is due in part to the diminution of edge sharpness by the photographic process and in part to the use of a 1.0 millimeter aperture on the densitometer (corresponding to a resolution of 2.65 miles on the lunar surface), which is larger than some of the small bright features on the photograph. As a result some small bright (or dark) features may be shown with a tone value somewhat more (or less) than their true value.

Morris (1963) attempted to correlate the relative tone measurements with normal albedo measurements that have been made by other investigators. Figure 2.9 shows a comparison made by the author of these albedo measurements



Blocked out area shown in Isotonal map of the Lansberg region of the Moon Figure 2.7. Isotonal map of the Lashowing configuration of contours. figure 2.8 at larger scale.

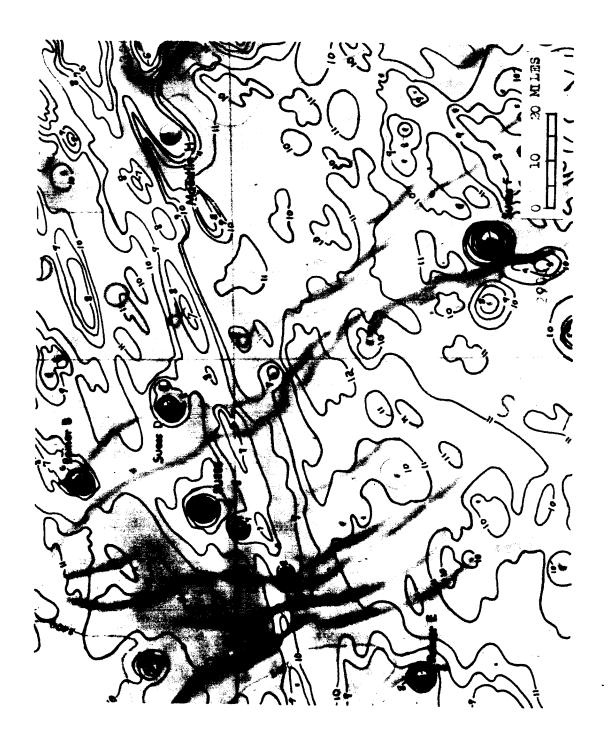
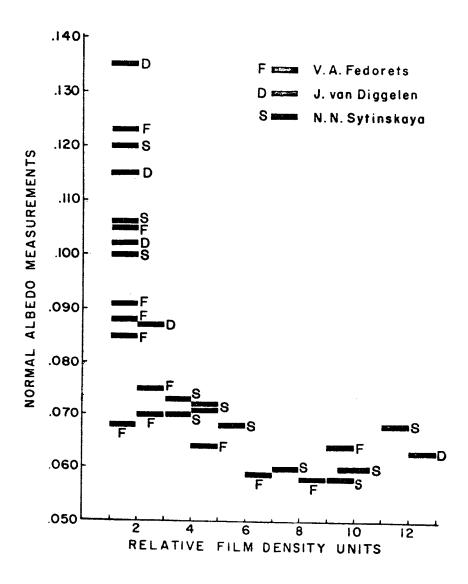


Figure 2.8. Part of isotonal map of the Lansberg region super-imposed on the U. S. Air Force chart.



Bigure 2.9. Comparis:n of 29 albeit measurements with this measurements made on the high-community film positive of the lausters region.

with relative tone values made in this study. A bar is used instead of a point for the albedo measurement because of the difficulty in properly locating them on the isotonal map, and also because the tone values may represent an integrated measurement of a specific albedo measurement integrated by the relatively large size of the densitometer aperture. There is a correlation between the darker tone measurements and the corresponding lower albedo measurements. However, as mentioned above, because of the restricted density range introduced by high-contrast development which has shifted the brighter tone values to the toe of the gamma curve, tone differences among the brighter areas are compressed and all albedo measurements above 0.085 are restricted to the first two density units.

Interpretations and conclusions

With due consideration to other criteria, tone values are an important key in interpretating the geologic data on lunar and terrestrial photographs. Similar tone values of widely distributed rock outcrops are often a clue to the correlation of such units. An isotonal map such as the one compiled in this study besides depicting small tone variations that would escape the unaided eye, and designating the brightest and darkest toned area, also correlates tones with a far greater precision than could be done visually. For example: In figure 2.3, A is the brightest tone measured while B is the darkest. C, D, E, and F are mare surfaces that all have the same tone value and may be areas of similar texture and chemical composition.

The dark area at G has the same tone value as what appears to be a lighter toned mare area at H. The surrounding brighter tones of G enhance its darkness and cause it to appear darker than H. The unaided eye cannot unambiguously recognize the same tone at different places on the photograph.

Although maria material is generally dark on lunar photographs, some is light enough to be confused with light toned ray material. The ray west of Kepler (see figure 2.2 at I) stands out quite clearly in combtrast to the darker maria. A ray of the same tone value would not be visible at location J since the mare surface in this area has the same general tone value as the ray. Only rays of a lighter tone value show up in this area. Thus, ray material although usually conspicuous where it overlays mare material has probably gone unrecognized in some smaller areas and is probably more extensive than has been supposed.

Tone variations on the lunar maria are not related to recognizable topography. This is readily apparent in figure 2.8 where isotonal lines of the darker mare material, not obscured by rays, cross the low mare ridges indiscriminately. This relationship suggests that these tone variations were present before the formation of the maria ridges. These variations are most likely the result of textural and compositional differences, and may be related to the age and genesis of the material. Although conclusive evidence is not available as to the exact nature of this material, a popular theory suggests an extrusive origin. The tone variations observed on the mare surfaces are not dissimilar to tone differences observed on terrestrial flows of basalt or welded tuff (Smith, 1960 and van Bandat, 1962, p. 57).

References

- Hackman, R. J., 1963, Isotonal map [of the Lansberg region of the Moon]:

 U.S. Geol. Survey, Astrogeologic studies annual progress report,

 August 25, 1961 to August 24, 1962, pt. A, p. 58-59.
- Kuiper, G. P., ed., 1961, Lunar atlas, v. 2: St. Louis, Mo., U.S. Air
 Force Aeronautical Chart and Information Center.
- Morris, E. C., 1963, Albedo measurements in the Lansberg region of the Moon: U.S. Geol. Survey, Astrogeologic studies annual progress report, August 25, 1961 to August 24, 1962, pt. A, p. 60-63.
- Smith, R. L., 1960, Zones and zonal variations in welded ash flows: U.S. Geol. Survey Prof. Paper 354-F, p. 149-159.
- Van Bandat, H. F., 1962, Aerogeology: Houston, Gulf Publishing Co., 350 p.



LUNAR INFRARED EMISSION STUDY

by Kenneth Watson

466 The earliest attempts to measure the lunar infrared emission (Rosse, 1869; Langley, 1887) indicated that the maximum surface temperature was about 370° K. The first reliable measurements of the emission during the daytime portion of lunation and during an eclipse were made by Pettit and Nicholson (1930) in 1927. Pettit (1940) remeasured the eclipse cooling near the center of the Moon's disc in 1939. The measurements were made with a vacuum thermocouple placed at the Newtonian focus of the 100-inch telescope. Galvanometer deflections were calibrated by measureing the shorter wavelength signal from comparison stars and extrapolating both the stellar radiation and thermocouple response to the 8-14 µ region. Several filters were used to measure the flux received over different wavelength regions. Pettit and Micholson's measurements showed that rapid surface cooling of the Moon occurs during the penumbral phase of the eclipse, which they concluded could be explained if the surface material were highly insulating. They also suggested that the lack of a significant variation between their measured brightness temperature from 9-11 \u03c4 and 8-14 \u03c4 implied that the surface material must be powdered in order to reduce the high reflectivity (and hence low emissivity) that silicate minerals posess in the nine micron region. An attempt to measure the radiation during the unlit portion of lunation yielded a temperature of 120° K, although the authors noted that the observed signal was near the lower limit of their detection system.

Shorthill (1962), while observing the eclipse cooling of several bright-ray craters with a thermistor bolometer during the 1960 eclipses of March and September, discovered that these craters cooled less rapidly than their surroundings. Sinton (1960) also observed the anomalous cooling of the bright ray crater Tycho during the September 1960 eclipse and suggested that the thickness of the dust layer in these bright ray craters, computed from eclipse cooling, could be used to provide relative ages of the craters. He also reported (1955) a midnight temperature of approximately 120° K for a fairly large area of the lunar disc.

In 1962, Murray and Wildey (1963 and 1964) scanned the unilluminated Moon using a more sensitive detection and calibration system than previous studies (Westphal et al., 1963). Their observations indicate that differences in thermal properties exist in localities on the Moon other than in the immediate vicinity of the large bright ray craters, and that the anomalous infrared radiation effects they detected persist well into the lunar nighttime. The observed lunation cooling, in areas where no significant anomalies are present, implies a midnight temperature of at least 20° K colder than the lower limit of detection of Pettit and Nicholson's observations.

Theoretical thermal models of the eclipse and lunation cooling of the Moon were first computed by Wesselink (1948). He assumed that the lunar surface was optically thick, that the emissivity was unity, and that the curvature of the Moon could be neglected because the penetration of the thermal energy is only a few centimeters. The one-dimensional heat conduction equation with constant thermal properties was applied using Stefan's law to construct a radiation boundary condition. The resulting partial differential equations were reduced to finite difference equations and solved by the Schmidt method. Wesselink concluded that the agreement between his model and Pettit's (1940) eclipse cooling observations indicates that the thermal properties of the Moon's surface layer are reasonably insensitive to temperature variations. His theoretical lunation cooling curve was computed with a thermal inertial of 970 cal⁻¹cm²sec^{1/2}deg^{1/2} because this value best fitted the eclipse cooling observations. The computed midnight temperature is about 20° cooler than the 120°K temperature measured by Pettit and Nicholson and by Sinton, but is not inconsistent with the observations of Murray and Wildey.

A model for the thermal conductivity of powders was suggested by Wesselink, in which the contact conduction of the grains was assumed negligible and the powder idealized as a series of radiating slabs. He concluded that the grain size of the powder must be less than 300 microns for radiative transfer to be negligible. Both the assumptions and conclusions of this model are at variance with the experimental investigation of selected silicate powders by the present author (Watson, 1964).

Jaeger and Harper (1950) and Jaeger (1953a) computed the eclipse and lunation cooling for a half space and also for a high impedance skin with

^{1/} The thermal inertia is defined equal to (kpc) 1/2, when k is the thermal conductivity, p the density, and c the specified heat.

negligible heat capacity overlying a half space, using the method of Laplace transforms. The assumption of constant thermal properties was acknowledged as a simplification. Jaeger (1953a) asserted that the eclipse observations cannot be explained by a conductivity with a temperature cubed dependence.

Muncey (1958) suggested that the variation of conductivity and specific heat is proportional to temperature. Although the solution of the heat conduction equation is fairly simple with this approximation, the temperature dependence chosen is not in agreement with either the thermal conductivity measurements of powders in vacuum (Watson, 1964) or the specific heats of silicates (Birth, 1942).

Infrared investigations to be carried out by the Branch of Astrogeology will utilize information obtained from the temporal and spectral distribution of the infrared emission to provide a more accurate
interpretation of the lunar surface geology. Close cooperation with the
lunar mappers of this branch will furnish a unique opportunity to compare
geologic type areas in their infrared emission properties.

Two main lines of evidence will be examined: Broad band emission from the Moon through the two major water vapor windows from 8-14 μ and 18-24 μ , and narrow band emission within these windows. The 18-24 μ window is superior to the 8-14 μ window in two respects: The emission from the Moon at 90 K is two orders of magnitude greater in this wavelength region, and the lack of an absorption band at the quartz reststrahlen maximum of 21 μ , whereas the 9 μ reststrahlen peak is obscured by the 9.6 μ ozone band.

The broad band emission studies will provide information on the distribution of thermal properties at and near the surface. Eclipse observations provide, at best, information concerning the upper few millimeters, whereas observations of the dark side of the Moon, near the morning terminator, provide information to a depth of several centimeters. No reliable observations have yet been successfully made in this latter region due to instrumental limitations.

Narrow band emission studies will primarily provide information on the grain size distribution of the lunar dust. If, in regions of thermal anomalies such as the bright ray craters, sufficiently large surfaces are exposed, or if there is only a very thin cover of dust, the narrow band emission studies will provide a limited amount of compositional analysis.

An important line of research which will be pursued will be the computation of useful models to explain the lunar infrared emission. The models will include lateral and vertical variations in thermal properties which are consistent with the surface geology, and inclusion of the temperature dependence of both the thermal conductivity and specific heat (see Watson, 1964). Both experimental and observational work is also planned, to extend present models of the visible reflectivity into the near infrared to provide a more accurate interpretation of the daytime lunar flux. In this connection, present studies are being made on the use of models of the lunar photometric function (Hapke, 1963) to derive the variation of absorbed solar energy as a function of the sun's elevation angle.

References

- Birch, A. F., Schairer, J. F., and Spicer, H. C., eds., 1942, Handbook of physical constants: Geol. Soc. America Spec. Paper 36, p. 223-266.
- Hapke, Bruce W., A theoretical photometric function for the lunar surface:

 Jour. Geophys. Res., v. 68, p. 4571-4586.
- Jaeger, J. C., 1953, The surface temperature of the Moon: Australian Jour.

 Physics, v.6, p. 10-21.
- Jaeger, J. C., and Harper, A. F. A., 1950, Nature of the surface of the Moon: Nature, v. 166, p. 1026.
- Langley, S. P., 1887, The temperature of the Moon: Natl. Acad. Sci. Mem., v. 4, p. 107-212 (1889).
- Muncey, R. W., 1958, Calculations of lunar temperatures: Nature, v. 181, p. 1458-1459.
- Murray, B. C., and Wildey, R. L., 1963, Stellar and planetary observations at 10 microns: Astrophys. Jour., v. 137, p. 692-693.
- Murray, B. C., and Wildey, R. L., 1964, Surface temperature variations during the lunar nighttime: Astrophys. Jour., v. 139, p. 734-750.
- Pettit, Edison, 1940, Radiation measurements on the eclipsed Moon: Astrophys.

 Jour., v. 91, p. 408-420.
- Pettit, Edison, and Nicholson, S. B., 1930, Lunar radiation and temperature:

 Astrophys. Jour., v. 71, p. 102-135.
- Rosse, Laurence (Earl of), 1869, On the radiation of heat from the Moon:
 Royal Soc. (London) Proc., v. 17, p. 436-443.

References--Continued

- Shorthill, R. W., 1962, Measurements of lunar temperature variations during an eclipse and throughout a lunation: Seattle, Boeing Sci. Research Labs. Doc. D1-82-0196, 21 p., 42 figs.; also in Conference on lunar exploration, Blacksburg, Va. 1962, Proceedings: Virginia Polytechnic Inst. Eng. Expt. Stat. Ser., no. 152, pt. A, paper VI, 63 p. (1963).
- Sinton, W. M., 1955, Observations of solar and lunar radiation at 1.5 millimeters: Optical Soc. America Jour., v. 45, p. 975-979.
- Sinton, W. M., 1960, Eclipse temperatures of the lunar crater Tycho:
 Lowell Observatory Bull., v. 5, no. 3, p. 25-26.
- Watson, Kenneth, 1964, I. The thermal conductivity measurements of selected silicate powders in vacuum from 150° 350° K. II. An interpretation of the Moon's eclipse and lunation cooling as observed through the Earth's atmosphere from 8-14 microns: unpublished doctoral thesis, California Institute of Technology.
- Wesselink, A. F., 1948, H at conductivity and nature of the lunar surface material: Astron. Inst. Netherlands Bull., v. 10, P. 351-363.
- Westphal, J. A., Murray, B. C., and Martz, D. E., 1963, An 8-14 micron infrared astronomical photometer: Applied Optics, v.2, p. 749-753.

DENSITY OF SMALL CRATERS ON THE LUNAR SURFACE

by H. J. Moore

Introduction

In order to make a successful landing on the Moon, we need reliable information on the roughness and form of the lunar surface features. Features smaller than one-half to one kilometer are not visible from the Earth through telescopes, so their nature must be inferred rather than observed directly.

The frequency of craters on the lunar surface can be predicted by combining current data on hypervelocity impact cratering with data on the distribution of interplanetary dust, micrometeoroids, meteoroids, and astroids. Such a prediction indicates that a lunar surface one billion years old composed of sand or rock could be virtually saturated with craters having diameters up to 10 meters, or possibly 100 meters. The prediction suffers from uncertainties, such as the frequency-size distribution of bodies that have impacted the surface of the Moon, the age of lunar surfaces, and the effects of impact on porous materials such as pumice or volcanic ash. Nevertheless, the prediction is useful because it suggests that the lunar surfaces should be rough on some scale less than 1 kilometer.

Mass and number of bodies impacting the lunar surface

The frequency of impacts on the Moon of interplanetary dust, micrometeoroids, and meteoroids 10^{-9} grams and larger have been estimated to

be about 10⁻⁵ impacts/meter²/sec (Beard, 1959, Whipple, 1961, 1963).
The frequency of impacts can be described by (Whipple, 1963):

$$N = 10^{-6.3} \text{ m}^{-1.0} \tag{1}$$

where:

N = the cumulative number of impacts/meter²/year with masses larger than m.

Equation (1) is valid for masses down to 10⁻⁹ to 10⁻¹⁰ grams and no further because solar radiation pressure should drive smaller particles from the Solar System (Whipple, 1958). In addition, the form of the curve for the influx distribution may change for masses of influx debris larger than 10⁶ grams (see for example, Brown, 1960). The effects of this variation for large masses will be neglected in this analysis.

A summary of estimates for the influx distribution (Beard, 1959; Whipple, 1958, 1961, 1963; Crozier, 1962; Alexander and others, 1962; Brown, 1960; Hawkins, 1959, 1961; Hawkins and Upton, 1958; van de Hulst, 1947; Watson, 1956) are shown in figure 4.1. Estimates yielding influx rates higher than equation (1) are taken to represent near-Earth concentrations.

A reasonable estimate of the mass ejected can be made from hyper-velocity impact data (Moore and Gault, 1963). An impact velocity of 15 km/sec will result in the ejection of 10³ grams for each gram of projectile, thus:

$$m = 10^{-3} 0 V$$
 (2)

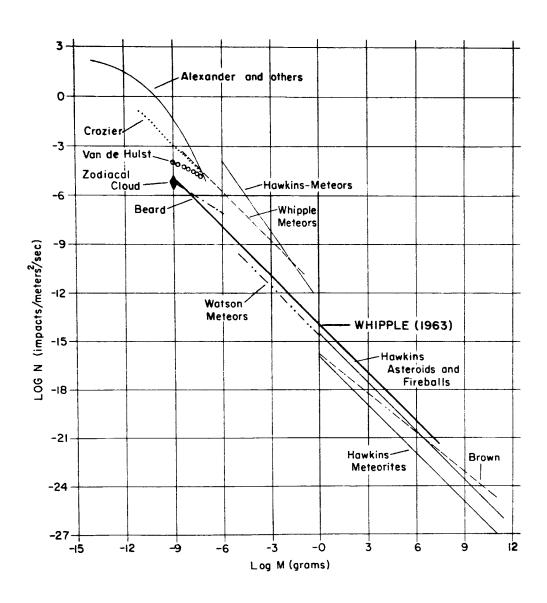


Figure 4.1. Cumulative frequency of impacts of bodies of mass m with the surface of the Moon.

where:

 ρ = the density of the ejecta V = the volume of ejecta.

In this model it is assumed that the mass ejected from a crater is directly proportional to the energy of the projectile. This is at least approximately true over the mass range of interest.

When the density of the ejecta is 1 g/cm³, the number of craters produced per square meter becomes:

$$N = 10^{-3.3} v^{-1}$$
 (3)

where V is the crater volume. For craters with the shape of a spherical segment with a depth-to-diameter ratio of 1 to 5:

$$V = 10^{-1.09} D^3$$
 (4)

so that

$$N = 10^{-2.21} D^{-3}$$
 (5)

where N is expressed in craters produced/meter²/year, and D is expressed in centimeters.

The lunar surface could be saturated by small craters in a short period. Expressing equation (5) in terms of crater area:

$$N = 10^{-2.21} \left(\frac{\pi}{4}\right)^{3/2} A^{-3/2}; \tag{6}$$

and, solving for the total area covered by craters gives:

$$\int_{A_1}^{A_2} A d(N) = 10^{-2.21} 3 \left(\frac{\pi}{4}\right)^{3/2} A^{-\frac{1}{2}} \begin{vmatrix} A_2 \\ A_1 \end{vmatrix}.$$
 (7a)

The total area of craters with diameters between 10^{-2} to 10^{-1} cm (ΔA) becomes:

$$\Delta A = 10^{0.02} \text{ cm}^2/\text{meter}^2/\text{year}. \tag{7b}$$

From equation (7b) it becomes apparent that craters with diameters between 10^{-2} to 10^{-1} cm could cover a lunar surface in 10^4 years.

If the period of micrometeoroid and meteoroid bombardment is increased, the craters must destroy each other by infilling, erosion, and superposition. The assumption that craters 2×10^3 cm deep and 10^4 cm across are destroyed by infilling and erosion in a billion years yields a crater destruction equation:

$$t = \frac{10^9}{10^4} D, (8)$$

where t is the maximum period in years that a crater or vestige of a crater with a diameter D_s in centimeters, can survive.

The form and magnitude of the crater destruction equation may be

partly justified by calculating the thickness of an ejecta layer that is expected to be deposited in a depression in a given period of time. For example, the largest projectile that can be expected to hit the Moon in a billion years may be obtained from equation (1). When the area of the Moon is taken as 4π (1.728 x 10^6 meters)² and the duration is 10^9 years, equation (1) becomes:

$$N_{Moon} = 10^{16.27} \text{ m}^{-1.0} \text{ impacts/Moon/billion years.}$$
 (9)

Since only one largest body is expected to impact the Moon, m becomes $10^{16.27}$ grams. Then from equation (9), the total mass flux for each square meter is:

$$\int_{\mathbf{m}_1}^{\mathbf{m}_2} \mathbf{m} \ d(\mathbf{N}) = \frac{10^{16.27} \ln \left(\frac{\mathbf{m}_1}{\mathbf{m}_2}\right)}{\text{area of Moon}}$$
(10)

where $m_1 = 10^{16.27}$ and $m_2 = 10^{-9}$; then,

$$\int_{m_1}^{m_2} m d(N) = 10^{4.33} \text{ grams/meter}^2/\text{billion years.}$$
 (11)

The gross ejected mass from equation (2) should be 10³ times larger than the influx mass, or 10^{7.33} grams/meter²/billion years. However, a significant portion of this mass is simply redistributed by impacts producing craters with depths smaller than the layer thickness. Since equation (5) predicts that saturation of the lunar surface should occur within a

billion years when the crater diameters are about 10^4 cm or depths are about 5×10^3 cm, these craters or slightly smaller craters will principally rework the pre-existing layer. Craters of this size are produced by projectiles with masses near 10^7 grams, so that roughly half of the gross ejected mass is simply reworked and the layer thickness is:

=
$$\rho 10^{7.03}$$
 grams/meter²/billion years (12a)

or, when ρ is taken as 1.0 g/cm³,

=
$$10^7 \text{cm}^3/\text{meter}^2/\text{billion years} =$$

 $10^3 \text{ cm/billion years}.$ (12b)

The depth of a crater that can be buried by this layer is complex because bouncing and saltation of grains will concentrate the debris in depressions. So if it is assumed that such a concentration is of the order of 2, then the depth of a crater that would be filled in a billion years is roughly 2 x 10^3 cm and the diameter is 10^4 cm, which is consistent with the crater destruction equation, e.g. (8).

The crater count for the saturated surface may be obtained as follows: differentiation of equation (5) yields:

$$d(N) = -10^{-1.73} D^{-4} d(D); (13)$$

multiplication by the crater destruction equation:

$$d(N)t = -10^{3.267} D^{-3} d(D);$$
 (14)

and integration from $D = \infty$ to $D = D_0$, yields the cumulative number of craters larger than diameter D_0 :

$$Nt = 10^{2.967} p_0^{-2}$$
 (15)

where Nt is expressed as craters/meter².

The cumulative area occupied by craters can be determined by expressing equation (15) as a function of crater area (A), differentiating this and then multiplying by A, and integrating:

$$\int A \ d(Nt) = -10^{2.967} \frac{\pi}{4} \ln \frac{A_2}{A_1}. \tag{16}$$

Because the slope of log (Nt) versus log D_O in equation (15) is -2, the area (ΔA) occupied by craters in each decade of diameters (D_O-19D_O) will be the same. For this case, A₁ = 100 A₂, so that

$$\Delta A = 10^{3.53} \text{cm}^2/\text{meter}^2$$
. (17)

The result is a billion-year-old lunar surface covered with craters of all sizes in various stages of destruction. Since equation (17) predicts that about 34 percent of the billion-year-old lunar surface might

be covered by craters and vestiges of craters in each interval D to 10 D, the area covered by recognizable craters in each interval D to 10 D is at least 10 percent (see fig.4.2). These craters vary from fresh craters to craters about three-tenths destroyed or obliterated by erosion and infilling.

Higher rates of crater destruction, which might result from flow of material or burial by volcanic products less than a billion years old, would substantially alter the above predictions. For example, if craters 10⁵ cm in diameter are destroyed in a billion years, the area covered by craters in each interval of D_o to 10 D_o would be only 1.0 to 2.0 percent. The crater distribution on a recently exposed volcanic flow would be of the form of equation (5) or a combination of equations (5) and (15). In the case of the combined equations, equation (5) would apply to the frequencies of larger craters and (15) to the frequencies of smaller ones.

The extreme predictions of the area occupied by craters are summarized in figure 4.2. The conservative theoretical estimate of 10 percent of the area occupied by craters with diameters of D_o to 10 D_o must join in some way with existing counts of craters larger than a kilometer in diameter. For this reason, craters between 10 and 100 meters might occupy 5 percent or less of the area; craters between 100 and 1000 meters, 2.5 percent or less. Such a change is consistent with the crater destruction equation (equation 15), in which craters larger than 100 meters are not destroyed in a billion years, so that a change in slope may be expected for craters between 10 meters and 1 kilometer in diameter.

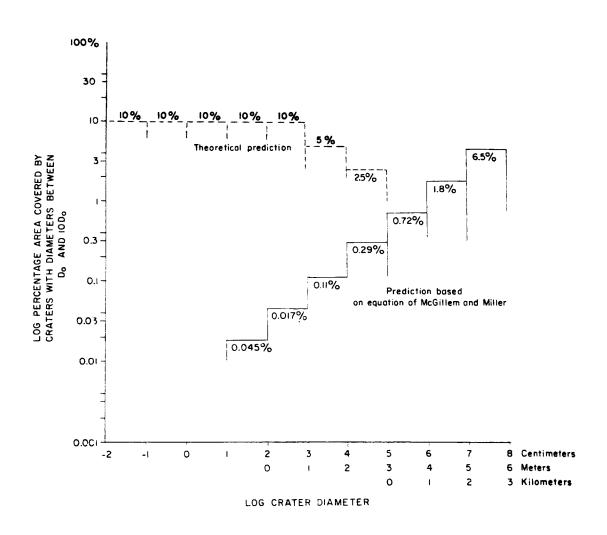


Figure 4.2. Predictions of area occupied by craters.

Density of secondary-impact craters

Secondary-impact craters may contribute to the surface roughness of the Moon, provided that the materials impacted are sufficiently weak. Data from hypervelocity impact cratering experiments with rock and sand targets indicate that about 50 percent of the kinetic energy of the impacting projectile will be imparted to the ejecta and 50 percent is dissipated in deforming and breaking the projectile and rock. A very small portion of ejecta with 25 percent of the projectile kinetic energy will be ejected from the Moon. The major portion of ejecta which remains on the Moon will contain 25 percent of the projectile kinetic energy as kinetic energy. The cumulative kinetic energy of the ejecta which remains on the Moon may be empirically expressed as follows (D. E. Gault, 1963, personal communication):

$$\frac{E_e}{E_p} = \left(-0.064 \log_{10} \frac{m_e}{M_e}\right) \tag{18}$$

where:

E = cumulative energy of the ejecta

 $E_{\mathbf{p}}$ = energy of the projectile

m = cumulative mass of ejecta

M = the total ejected mass.

Equation (18) is only valid for $1 \ge \frac{m_e}{M_e} \ge 10^{-3.91}$.

Detailed studies of high-speed photographs of ejecta from craters during crater formation show that the size of fragments ejected increases with time (see for example, Gault, Heitowit, and Moore, 1963, figs. 1 through 7). The material initially ejected with high velocities is of the order of a few tenths of a micron. Ejecta fragment sizes increase so that intermediate size fragments are ejected with intermediate velocities and finally the largest fragments are ejected with low velocities. Because the velocity of ejected fragments varies regularly with the amount of material ejected and the fragment size (see Gault, Shoemaker, and Moore, 1963, fig. 10, p. 37), the size distribution equation for the ejecta may be substituted in equation (18). The size distribution equation (Gault, Shoemaker, and Moore, 1963, p. 5, figs. 2, 3, p. 26, 27, 28) is:

$$\frac{\mathbf{m}_{\mathbf{c}}}{\mathbf{M}_{\mathbf{e}}} = \left(\frac{\mathbf{m}}{\mathbf{m}_{\mathbf{b}}}\right)^{\alpha} \tag{19}$$

where

 m_c = the cumulative mass finer than size m (measured in terms of mass)

m = the mass of the largest fragment.

When m = m and $\alpha = 0.25$, equation (18) becomes:

$$E_e = E_p \left[-0.016 \log_{10} \frac{m}{m_b} \right].$$
 (20)

This may also be expressed in terms of the frequency of fragments.

From equation (19):

$$d(m_c) = \frac{M_c}{m_b} 0.25 \text{ m}^{-0.75} d(m); \qquad (21)$$

and from experimental data for small craters (Gault, Shoemaker, Moore, 1963, p. 9):

$$M_e = 10 m_b$$
.

Then,

$$d(m_c) = 10 m_b^{0.75} 0.25 m^{-0.75} d(m).$$
 (22)

In order to obtain the differential frequency d(f), $d(m_c)$ is divided by m:

$$d(f) = \frac{d(m_c)}{m}; \qquad (23)$$

and,

$$d(f) = 10 \, m_b^{0.75} \, 0.25 \, m^{-1.75} \, d(m).$$
 (24)

Integration of equation (24) gives the cumulative frequency (f):

$$f = -10 m_b^{0.75} \frac{0.25}{0.75} m^{-0.75} m_b^{m}$$
 or,

$$f = 3.33 \left[\frac{m}{m_b} \right]^{-0.75}$$
 (25)

for $m \ll m_h$

$$f \approx 3.33 \left(\frac{m}{m_b}\right)^{-0.75}; \tag{26}$$

then from equation (25):

$$E_e = E_p \left(0.0214 \log_{10} \left(\frac{f}{3.33} + 1 \right) \right),$$

or for large values of f:

$$E_e \approx E_p \ (0.00933 \log_e f).$$
 (27)

Equation (27) is only valid to $f = 10^{12.22}$ because equation (8) is only valid to $\frac{m}{M_{\odot}} = 10^{-3.91}$.

Differentiation of equation (27) yields:

$$\frac{d(E_e)}{d(f)} = \frac{E_p (0.00933)}{f}.$$
 (28)

When d(f) is set equal to one, $d(E_e)$ represents the energy of one fragment:

$$d(E_e) = E_p (0.00933)f^{-1}$$
. (29)

If the velocity of influx debris to the lunar surface is taken as constant, equation (1) can be expressed in terms of energy:

$$E_{\mathbf{p}} = \frac{V^2}{2} m = 10^{-6.3} N^{-1}, \tag{30}$$

so that equations (29) and (30) have the same form.

When the yield is the same for primary and secondary impact craters, the cumulative frequency of secondary impact craters from one primary impact crater is:

$$\frac{V_{s}}{V_{p}} = 9.33 \times 10^{-3} f^{-1}$$
 (31)

when

 V_s = the volume of secondary impact crater V_p = the volume of primary impact crater P_p f = cumulative frequency of secondary impact craters larger than V_s .

If there are N primary impact craters, equation (31) should be multiplied by N:

$$Nf = N 9.33 \times 10^{-3} V_p V_s^{-1}$$
. (32)

The secondary craters from impacts larger than V_p can be summed for 12.22 intervals of $\Delta \log_{10} f = 1.0$ because equations (29) and (30) have

the same form and equation (27) is only valid to $f = 10^{12.22}$; then,

$$\frac{\Sigma Nf}{N} = 1.14 \times 10^{-1}$$
 (33)

for primary and secondary impact craters that are the same size. Therefore, primary impact craters should, in general, be about 10 times as abundant as secondary impact craters of the same size. A multitude of secondary impact craters that are smaller than the smallest primary impact crater should be present on the Moon because most of the ejected fragments produce secondary craters smaller than the primary craters.

Equations (29) and (31) indicate that younger primary impact craters, such as Tycho, Copernicus, and Aristarchus, should have hummocky ejecta blankets and rays due to secondary impacts.

Conclusions

1. The frequency of small craters on the lunar surface predicted on the basis of the influx of interplanetary debris indicates a high density of craters up to 10 meters across can be expected on billion-year-old lunar surfaces composed of rock or sand. Ten percent of the total area of the surface could be covered by well preserved craters between 1 to 10 meters across, 10 percent of the total surface covered by well preserved craters between 0.1 and 1 meter across, and 10 percent by well preserved craters between 0.01 and 0.1 meter across.

2. Comparison between theoretical predictions for small crater frequencies on the lunar surface and small crater frequencies predicted by extrapolation of crater counts of large craters differ significantly and indicate extrapolated crater counts are probably invalid.

References

- Alexander, W. M., McCracken, C. W., Secretan, L., and Berg, O. E., 1962,
 Rocket, satellite, and space-probe measurements of interplanetary
 dust; Am. Geophys. Union Trans., v. 43, no. 3, p. 351-360.
- Beard, D. B., 1959, Interplanetary dust distribution: Astrophys. Jour., v. 129, p. 496-506.
- Brown, Harrison, 1960, The density and mass distribution of meteoritic bodies in the neighborhood of the Earth's orbit: Jour. Geophys.

 Research, v. 65, no. 6, p. 1679-1683; addendum: v. 66, no. 4, p. 1316-1317.
- Crozier, W. D., 1962, Five years of continuous collection of black, magnetic spherules from the atmosphere: Jour. Geophys. Research, v. 67, no. 6, p. 2543-2548.
- Gault, D. E., Heitowit, E. D., and Moore, H. J., 1963, Some observations of hypervelocity impacts with porous media: U.S. Natl. Aeronautics and Space Adm. Tech. Memo. X-54,009, 20 p., 17 figs.
- Gault, D. E., Shoemaker, E. M., and Moore, H. J., 1963, Spray ejected from the lunar surface by meteoroid impact: U.S. Natl. Aeronautics and Space Adm. Tech. Note D-1767, 39 p.

References--Continued

- Hawkins, G. S., 1959, The relation between asteroids, fireballs, and meteorites: Astron. Jour., v. 64, no. 1275, p. 450-454.
- Hawkins, G. S., 1961, Asteroidal fragments: Lunar and Planetary Exploration Colloquium Proc., v. 2, no. 4, p. 5-11.
- Hawkins, G. S., and Upton, E. K. L., 1958, The influx rate of meteors in the Earth's atmosphere: Astrophys. Jour., v. 128, no. 3, p. 727-735.
- McGillem, C. D., and Miller, B. P., 1962, Lunar surface roughness from crater statistics: Jour. Geophys. Research, v. 67, no. 12, p. 4787-4794.
- Moore, H. J., and Gault, D. E., 1963, Relations between dimensions of impact craters and properties of rock targets and projectiles:U.S. Geol. Survey, Astrogeologic studies annual progress report,Aug. 25, 1961 to Aug. 24, 1962, pt. B, p. 38-79.
- van de Hulst, H. C., 1947, Zodiacal light in the solar corona: Astrophys. Jour., v. 105, no. 3, p. 471-488.
- Watson, F. G., 1956, Between the planets: Cambridge, Mass., Harvard Univ. Press, 188 p.
- Whipple, F. L., 1958, The meteoritic risk to space vehicles, in Alperin, Morton, and Gregory, A. F., eds., Vistas in astronautics, v. 1:

 New York, Pergamon Press, p. 115-124.
- Whipple, F. L., 1961, The dust cloud about the earth: Nature, v. 189, no. 4759, p. 127-128.
- Whipple, F. L., 1963, On meteroids and penetration: Jour. Geophys.

 Research, v. 68, no. 17, p. 4929-4939.

1500°

CHANGE OF EFFECTIVE TARGET STRENGTH WITH INCREASING

SIZE OF HYPERVELOCITY IMPACT CRATERS

by H. J. Moore, D. E. Gault $\frac{1}{2}$, and E. D. Heitowit $\frac{1}{2}$

Introduction

Experiments with hypervelocity and high-velocity projectile impacts on rocks are being made by the U.S. Geological Survey and the Ames Research Center of the National Aeronautics and Space Administration. This paper presents and discusses the results obtained from 38 impact experiments using basalt as a target material.

The experimental data show that the mass ejected (M_e) from craters produced by hypervelocity and high-velocity projectile impact with basalt increases with the projectile energy (E_p), the square root of the ratio of projectile and target density ($[^pp/\rho_t]^{\frac{1}{2}}$), and the size of the resulting crater (M_e). The amount of mass ejected for each unit of projectile energy that has been corrected for the density ratio ($M_e/[^pp/\rho_t]^{\frac{1}{2}}E_p$) increases with the size of the resulting crater (M_e).

Theoretical predictions for the mass ejected during crater formation by hypervelocity projectile impacts with materials of constant strength (Charters and Summers, 1959) are not consistent with the results. This theory indicates that the amount of mass ejected for each unit of projectile energy that has been corrected for the density ratio $(M_e/[^pp/\rho_t]^{\frac{1}{2}}E_p)$ should be constant. In addition, theoretical predictions for the mass

^{1/} Ames Research Center, National Aeronautics and Space Administration.

ejected during crater formation by low velocity impacts with materials of constant strength (Hartman, 1959) are not consistent with the results. The low velocity impact cratering theory predicts M_e/E_p should be constant.

If the strength of the target material decreases with increasing size of the resulting crater (M_e) according to the Griffith crack theory (Griffith, 1924) or the weakest-link theory of failure for flawed mater-ials (Evans and Pomeroy, 1958), the experimental results can be explained.

Experimental conditions and results

Aluminum, steel, and polyethylene projectiles weighing between 0.0058 and 4.051 grams were fired in an atmosphere of air or nitrogen at pressures from 2 to 75 mm of mercury using light-gas guns (Charters, Denardo, and Rossow, 1957) at the Free Flight Range of the Ames Research Center, Moffett Field, California. Spherical projectiles and cylindrical polyethylene projectiles with a diameter-length ratio near 1.6 were employed. Metal projectiles were mounted in nylon sabots, which guided the projectiles down the launching tube and were separated from the projectiles after launch by aerodynamic drag. Projectile velocities at impact were determined by spark photographs of the projectiles in flight to within ± 0.01 kilometers/ second. Projectile velocities ranged between 0.88 and 7.3 kilometers/ second and projectile energies ranged between 4.9 at 10⁸ and 7.4 x 10¹¹ ergs. The projectiles in the 38 experiments impacted planed rock surfaces of basalt at normal incidence.

Sawed blocks of unweathered basalt, free of visible flaws, were used for target materials. The basalt was obtained from Putnam Peak near Vacaville, California and from Buckboard Mesa, Nevada Test Site. Most of the targets were basalt from Putnam Peak with densities between 2.70 and 2.89 g/cm³. A few experiments used basalt from Buckboard Mesa with densities between 2.55 and 2.72 g/cm³. Compressive strengths, measured using 1" x 1" x 2" rectangular blocks of basalt, averaged 2.56 x 10% dynes/cm² and ranged between 1.56 x 109 and 3.69 x 109 dynes/cm². The computed average shear strength is 8.6 x 108 dynes/cm² when the angle of internal friction is taken as 48 degrees. Measured tensile strengths using 1/2" x 1/2" x 6"rods averaged 1.42 x 108 dynes/cm² and ranged between 0.90 x 108 and 2.32 x 108 dynes/cm². Acoustic velocities for the basalt from Putnam Peak averaged near 5.5 kilometers/second and 4.9 kilometers/second for basalt from Buckboard Mesa.

The mass of basalt ejected from each crater was determined by (1) weighing the target block before and after impact, (2) weighing the recovered ejecta, (3) multiplying target density by crater volume, and (4) a combination of these methods. Crater volumes used in computing ejected mass were determined by planimetric measurements of topographic maps of the craters. The topographic maps were prepared using photogrammetric techniques (Lugn, 1964). Comparisons between the three methods of determining ejected mass gave results agreeing within 10 percent.

A least-squares fit to the data from the 38 experiments (see solid line in fig. 5.1), where the ejected mass was taken as the dependent

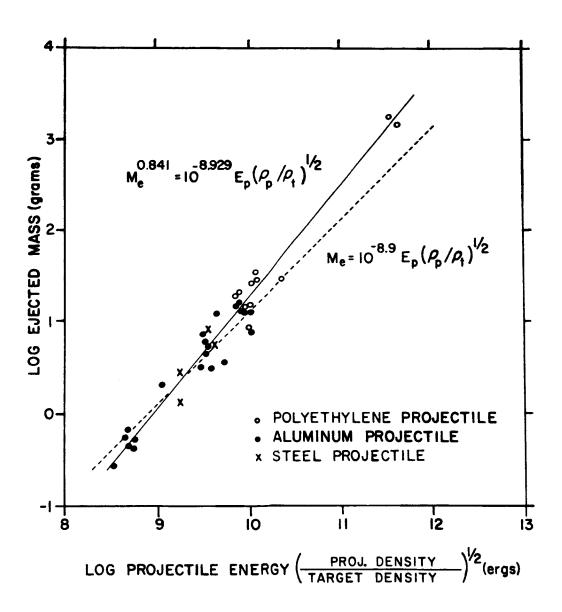


Figure 5.1. Experimental relationship between ejected mass and projectile properties. Solid line represents least-squares fit to experimental data. Dashed line represents theoretical predictions for material with constant strength.

variable, indicates the following relationship:

$$M_e = 10^{-10.613} \left[\left(\frac{\rho_p}{\rho_t} \right)^{\frac{1}{2}} E_p \right]^{1.189}$$
 (1a)

where:

 M_e = ejected mass E_p = projectile energy ρ_p = projectile density ρ_r = target density.

Equation (a) may be recast:

$$M_e^{0.841} = 10^{-8.929} \left[\frac{\rho_p}{\rho_+} \right]^{\frac{1}{2}} E_p$$
 (1b)

The exponent of M_e in equation 1b differs significantly from 1.000.

Calculations of the confidence limits using the t-test for the data

(Kenney and Keeping, 1951, pt. 2, p. 208-211) for the exponent of M_e at the 99 and 95 percent level are:

$$P \left\{ 0.771 \leq 0.841 \leq 0.925 \right\} = 0.99$$

and,

$$P \left\{ 0.789 \le 0.841 \le 0.901 \right\} = 0.95.$$

The multiplication of the parameter $({}^{\rho}p/{}_{\rho_t})^{\frac{1}{2}}$ and the projectile energy (E_p) effectively reduces the scatter of the data for the hypervelocity impact experiments using basalt, as well as those using metal targets (Summers, 1959).

Target strength

The conditions of target failure during the formation of craters produced by hypervelocity and high-velocity projectile impact are complex. Failure occurs under high to low confining pressures (Moore, MacCormack, and Gault, 1963). In addition, part of the materials ejected during crater formation is composed of fused projectile and target material (unpublished data; see also, Shoemaker, Gault, Moore, and Lugn, 1963). However, the effective deformation strength (S) of the target basalt during crater formation resulting from hypervelocity and high-velocity projectile impact is, in part, related to the tensile and compressive strengths of the basalt because the fractures in most of the ejected fragments are typical of both types of failure (see for example, Moore, Gault, and Lugn, 1962). Comparison between hypervelocity and high-velocity impact craters in metals and temporary craters in water produced by falling water drops reveal that tensile failure plays a dominant role in crater formation in basalt (Moore, MacCormack, and Gault, 1963). The low tensile strength of basalt permits spalling, which results in craters that are about 10 times as large as craters in metals and temporary craters in water when their respective projectile emergies are corrected for their respective deformations strengths during compressive failure (Moore, MacCormack, and

Gault, 1963). This difference can be accounted for by tensile failure of the basalt during crater formation and lack of tensile failure during crater formation of most metals and water.

Change in strength with size

Measured strengths of materials may decrease with an increase of sixe of the test specimen. Change of strength with change of size of the test specimens for brittle materials is a well established fact (see for examples, Evans and Pomeroy, 1958; Fisher and Holloman, 1947, p. 559-560).

A simple explanation for the change of strength for a limited case may be derived from the Griffith theory of failure (Griffith, 1924), where the condition for failure is:

$$R = m c^{-\frac{1}{2}}$$
 (2)

where:

R = rupture stress normal to the direction of
 a crack or defect

m = constant for the material

c = crack or defect length.

If the crack length along which failure occurs is assumed to be directly related to the size of the test specimen (x), the rupture stress can be related to the size of the test specimen:

$$R \propto x^{-\frac{1}{2}}$$
 (3a)

or to the volume (Vol) and mass (M) of the test specimen:

$$R \propto \text{Vol}^{-.167} \tag{3b}$$

$$R \propto M^{-0.167}$$
. (3c)

The weakest-link theory (Evans and Pomeroy, 1958), which is a statistical solution to the problem of change of strength with size for materials with defects or cracks, yields R α x $^{-\frac{1}{2}}$ (equation 3a) when the material contains Griffith flaws; and R α x 0 when the material is unflawed. The value of rapture stress may vary between these two predictions, depending on the nature and activation of the flaws in the specimen.

The compressive strength of cubes of coal varies with the size of the cube, according to static measurements made by Evans and Pomeroy (1958, p. 7), with a ball-and-plane crushing device. Their results were in excellent agreement with equation (34). The exponent for x was -0.52 ± 0.02 instead of 0.5 or 1/2.

Explanation of experimental results

The fluid impact theory of Charters and Summers (1959) predicts that the crater volume or ejected mass, for projectiles and targets of given materials, should be proportional to the projectile energy. The Charters-Summers equation, modified to obtain ejected mass, is:

$$M_{e} = \frac{E_{p}}{2} \frac{\rho_{t}}{S}$$
 (4a)

where S = the effective deformation strength of the target. This equation, modified for density ratios in accordance with experimental data (Summers, 1959, p. 5) is:

$$M_{e} = \left(\frac{\rho_{p}}{\rho_{t}}\right)^{\frac{1}{2}} \left(\frac{E_{p}}{2}\right) \left(\frac{\rho_{t}}{S}\right). \tag{4b}$$

Predictions based on equation (4b) are indicated with a dashed line in figure 5.1.

The Charters-Summers theory assumes the effective deformation strength (S) is constant. If, however, it is assumed that the effective deformation strength (S) changes according to equation (3c), then:

$$S = k M_e^{-0.167}$$
 (5)

where k is a constant. Substitution into equation (4b) yields an exponent for M close to the experimentally determined exponent of M (0.841) when the values of ρ_{t} and k are considered to be constant:

$$M_{e}^{0.833} = \left(\frac{\rho_{p}}{\rho_{r}}\right) \left(\frac{E_{p}}{2}\right) \left(\frac{\rho_{t}}{k}\right). \tag{6}$$

The theory of crater formation by the impact of drill bits (Hartman, 1959) also assumes that the deformation strength of the target material is constant and that the mass ejected (or crater volume) for a given material is directly proportional to the energy of the drill bit. The experimental results for craters produced by the impact of hemispherical drill bits do not concur with the theory but yield values for the exponent of the drill bit energy larger than one and near 1.2 (Hartman, 1959). This result is consistent with equation (6).

Conclusions

The experimental results show that the mass ejected (M_e) from craters produced by hypervelocity and high-velocity projectile impact with basalt increases with the projectile energy (E_p), the square root of the ratio of projectile and target density ($[^{\rho}p/\rho_{t}]^{\frac{1}{2}}$), and the size of the resulting crater (M_e). The amount of mass ejected for each unit of projectile energy that has been corrected for the density ratio (M_e/ $[^{\rho}p/\rho_{t}]^{\frac{1}{2}}$ E_p) increases with the size of the resulting crater (M_e).

This result is consistent with a decrease of the effective target strength of the basalts with increasing size of the resulting craters.

References

Charters, A. C., Depardo, B. P., and Rossow, V. V., 1957, Development of a piston-compressor type light-gas gan for the launching of free-flight models of high velocity's U.S. Natl. Advisory Comm. Aeronautics Tech. Note 4143, 95 p.

References -- Continued

- Charters, A. C., and Summers, J. L., 1959, Some comments on the phenomenon of high-speed impact, in Decennial symposium, May 26, 1959, White Oak U.S. Naval Ordnance Lab., Silver Spring, Md., p. 1-21.
- Evans, I., and Pomeroy, C. D., 1958, The strength of cubes of coal in uniaxial compression, in Walton, W. H., ed., Mechanical properties of non-metallic brittle materials: New York, Interscience, p. 5-25.
- Fisher, J. C., and Hollomon, J. H., 1947, A statistical theory of fracture:

 Am. Inst. Mining Metall. Petroleum Engineers Trans., v. 171, p. 546561.
- Griffith, A. A., 1924, The theory of rupture: Internat. Cong. Applied Mechanics Proc., Delft, p. 55-63.
- Hartman, H. L., 1959, Basic studies of percussion drilling: Mining Eng., v. 11, p. 69-75.
- Kenney, J. F., and Keeping, E. S., 1951, Mathematics of statistics, pt. 2, 2nd ed.: New York, Van Nostrand, 429 p.
- Lugn, R. V., 1964, Photogrammetric mapping of experimental craters: Photogramm. Eng., v. 30, no. 1, p. 55-58.
- Moore, H. J., Gault, D. E., and Lugn, R. V., 1962, Experimental hyper-velocity impact craters in rock: Symposium on hypervelocity impact, 5th, Denver 1961, Proc., v. 1, pt. 2, p. 625-643.
- Moore, H. J., MacCormack, R. W., and Gault, D. E., 1963, Fluid impact craters and hypervelocity-high-velocity impact experiments in metals and rock: Symposium on hypervelocity impact, 6th, Cleveland, Ohio, 1963, Proc., pt. 2, v. 2, p. 367-399.

References--Continued

- Shoemaker, E. M., Gault, D. E., Moore, H. J., and Lugn, R. V., 1963,

 Hypervelocity impact of steel into Coconino Sandstone: ... Am. Jour.

 Sci., v. 261, p. 668-682.
- Summers, J. L., 1959, Investigation of high-speed impact -- regions of impact and impact at oblique angles: U.S. Natl. Aeronautics and Space Adm. Tech. Note D-94, 18 p.



PHOTOGRAMMETRIC MAPPING OF EXPERIMENTAL

CRATERS

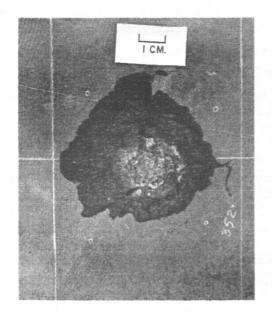


by R. V. Lugn

Introduction

One of the projects being conducted by the Branch of Astrogeology, U.S. Geological Survey, is the study of small experimental impact craters. This is a cooperative venture with the Planetary Science Branch of the Space Sciences Division and Free Flight Range at the Ames Research Center of the National Aeronautics and Space Administration.

At Ames Research Center small craters are produced by projectiles with velocities up to 23,000 feet per second. The resulting craters range in diameter from less than one centimeter to more than four centimeters. Photogrammetric techniques are employed to make topographic and structural maps of the experimental craters. From these maps the craters are measured, their volume computed, and their structure displayed. The maps are obtained from stereoscopic pairs of photographs (fig. 6.1) adapted for use in a plotting instrument of the double-projection analyphic type (Thompson, 1958). The methods used in mapping the small craters are essentially the same as those used in conventional aerial mapping projects.



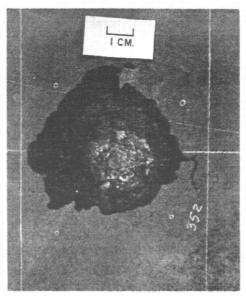


Figure 6.1. Stereoscopic pair of photographs of an experimental crater in basalt.

Procedure

Photo scale and map scale vary with the size of the crater; the map scale must be large enough to show topography and structure clearly. The maps are compiled at stereo model scale and, if desired, reduced photographically for publication. Comparing intervals are chosen that best illustrate the topography. No formal accuracy requirement has been set; measurements made on the map with an ordinary centimeter scale must correspond with those made on the original crater.

Before plotting contours it is necessary to establish central points on the crater that can be recognized on the photographs. This is done my marking the smooth surface of the target block with colored pencil; if the surface is rough, as in the case of sandstones, lines are made with thread. One line is drawn through the center of the crater, extending across the target block as far as possible. This line corresponds with the flight line in aerial photography. Two other lines are drawn at the edges of the crater, perpendicular to the "flight line." The two intersections are considered the principal points of the stereo pair of photographs to be taken. Four dots are also made at the corners of a square enclosing the crater. From these points, measurements are made on the target block to determine the map scale.

In taking the photographs it is necessary to use a camera that has an adjustable image distance, because the objective distance in all cases is finite. The camera used is a view type with 4" x 5" format. Lenses with 90-mm or 135-mm focal length are commonly used.

The target block to be photographed is set up so that the target face which includes the crater is a horizontal plane. The camera is then positioned over the block and leveled so that the film plane is also horizontal. With a view camera the ground glass is centered over one of the intersections formed by the lines drawn on the target block. The crater is then brought into focus by moving the camera vertically. The field of view is such that one of the intersections on the target block coincides with the principal point of the camera, and the other intersection lies about five centimeters to one side. After one photograph has been taken in this position, the camera or the target block, whichever is more convenient, is moved along the "flight line" until the second intersection coincides with the principal point of the camera, and another exposure is made. The two photographs give complete stereo coverage of the crater.

No available stereoplotting instrument accommodates the geometry of the camera. The Er-55-was chosen because it gives the desired amount of magnification, and because it is more convenient to make ER-55 diapositives than any other kind.

The diapositives are made with a Beseler printer. The negative is placed in the printer and the image positioned with one principal point in the center of the diapositive plate and the other not more than four centimeters to one side. Thus both principal points are included in the projected stereo model. The two diapositives are then placed in the ER-55 projectors, a parallax solution obtained, and absolute orientation achieved.

Because the stereoplotter and camera are not compatible in regard to a horizontal-vertical scale ratio of one, it is necessary to convert the vertical scale to the same value as the horizontal scale (Marsden, 1952). This can be done either mathematically or empirically.

In the mathematical method the vertical scale is determined by dividing the projection distance of the projector (PD_p) by the objective distance of the camera (OD_p) :

$$\frac{PD_p}{OD_c}$$

The horizontal scale is determined by dividing the product of the projection distance of the projector and the image distance of the camera (ID_c) by the product of the objective distance of the camera and the image distance of the projector (ID_p) , and multiplying the answer by the reduction of the Beseler printer (R):

$$\frac{(PD_p) (ID_c)}{(OD_c) (ID_p)} R$$

These calculations give approximate vertical and horizontal scales. During the diapositive printing stage, the scale ratio can be adjusted to approximately 1:1, since only the horizontal scale is dependent on R. More precise mathematical determinations could be made if the image and objective distances of the camera and projectors could be measured accurately.

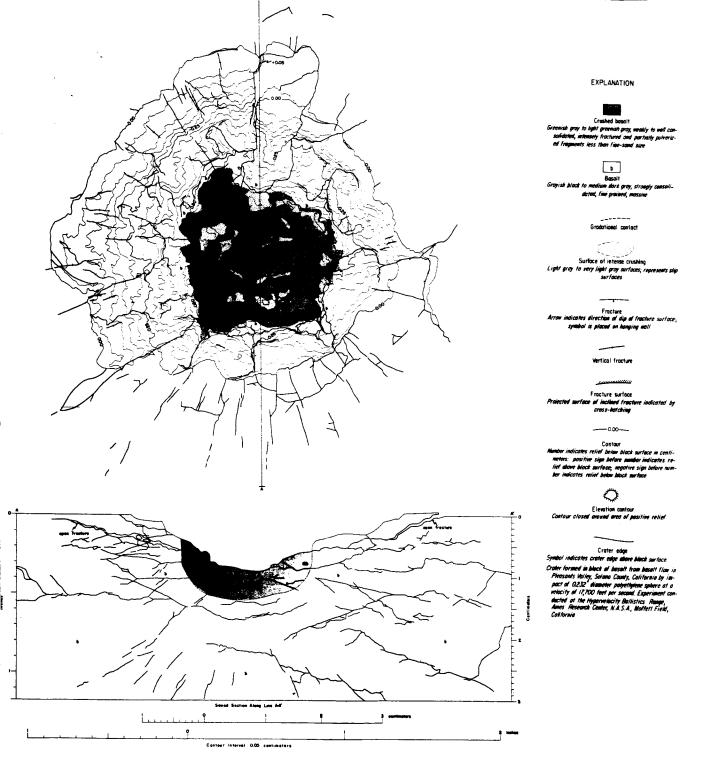


Figure 6.2. Topographic and structural map of hypervelocity impact crater in basalt.

In the experimental cratering program it has been found satisfactory to determine vertical and horizontal scale empirically by comparing measurements made on the stereo model with corresponding measurements on the crater itself. Mathematical methods may be substituted later in the program.

A map is compiled at the scale of the stereo model. The topography and structure are compiled separately on two registered pieces of scribe-coat base. From these base maps positives are made. Usually a cross section is constructed. Figure 6.2 is a topographic and structural map of an experimental crater in basalt.

Crater volumes have been obtained from the topographic maps with a compensating polar planimeter, and compared with volumes obtained by filling the craters with Ottawa sand. In some of these tests the two measurements were the same; in others, they differed by as much as ten percent. The average difference is about two percent. The maps allow three-dimensional measurement of craters and provide accurate representation of crater form and structure.

References

- Maraden, L. E., 1952, Experimental focal length variation for multiplex plotting: U.S. Geol. Survey Topo. Div. Bull., v. 2, no. 1,
 p. 5-7.
- Thompson, M. M., 1958, Photogrammetric mapping of sand beds in a hydraulic test flume: Photogramm. Eng., v. 24, no. 3, p. 468-475.

PHOTOGRAPHIC AND PHOTOELECTRIC INVESTIGATIONS OF THE EARTH-MOON LIBRATION REGIONS L_4 & L_5 FROM MT. CHACALTAYA, BOLIVIA

bу

E. C. Morris, J. Ring, and H. G. Stephens

Photographic and photoelectric investigations of the L₄ and L₅ libration regions, which were begun in the summer of 1962 from Mt. Chacaltaya, Bolivia, (Morris and Stephens, 1963), were continued during the summer and fall of 1963. The investigations were initiated to determine the possible existence of clouds of dust or particulate matter in the orbital path of the Moon, 60° ahead of and 60° behind the Moon. K. Kordylewski, of Krakow University, reported having photographed faintly luminous cloud-like objects in these regions in the spring and again in the fall of 1961 (Kordylewski, 1961a and 1961b); however, his observations have never been adequately verified.

The libration points, also known as Lagrangian points (Lagrange, 1776), are points of equalibrium, where centrifugal forces balance the gravitational forces. Particles would tend to remain at these points indefinitely unless they are perturbed by other forces. However, clouds of particles in the libration regions may only be transient, because of perturbing forces of the sun and planets. The supply of matter to the libration regions probably is derived from particles ejected from the Moon by hypervelocity impact of asteroidal and cometary particles (Shoemaker, 1962); therefore particles are moving continuously in and

out of the libration regions: when the supply is high, the particle density increases and the clouds may be visible due to increased reflection of sunlight, but during times of low particle density the clouds will not be visible.

The observational program for 1963 was planned for continuous photographic surveillance of the $\rm L_4$ and $\rm L_5$ regions in order to detect any increase in brightness that would make the clouds visible.

Photographic observations were made with a 12-inch focal length K 37 aerial camera adapted to take 8" x 10" cut film or glass plates. The photographs covered a sky area of 45 by 37 degrees. The camera was mounted on an equatorial mount that was driven at sidereal rate. A long wave length filter at 4500 Å and Eastman Kodak 103 0 spectroscopic plates were used to gain maximum contrast between sunlight reflected from the dust particles and nightglow.

During the period of June 1963 to November 5, 1963, 17 photographic plates of L_4 and 28 plates of L_5 were taken. Visual examination of the photographic plates showed no significant increase of density in areas of the libration points. Twenty of these plates were traversed with a recording microphotometer at one-half degree intervals over a 10 degree area centered at the libration points. No departures from the mean density of the background sky were detected. Ten of the best plates, which have the highest probability of yielding information on particle density within the libration regions, will be statistically analysed at 0.1 degree intervals. These plates will be calibrated to absolute measurements made with the photoelectric observations.

Photoelectric observations were made during the latter part of July with a 6-inch diameter Maksutov-Cassegrain telescope mounted in altazimuth and equipped with a motor drive to turn it in azimuth at a rate of 5 degrees per minute. An aperture in the focal plane allowed light from a field one-half degree in diameter to pass through an interference filter, centered on H (4861 Å) with a half-width of 20 Å, onto a photomultiplier tube. The signal from the photo multiplier was recorded on a strip chart recorder after dc amplification. The interference filter was used because previous observations have indicated that H is a suitable wavelength region to maximize the contrast between sunlight scattered by the dust and nightglow. The signal from the night sky yielded a current of 10^{-9} amps which is two orders of magnitude greater than the multiplier dark current.

Raster scans of the sky covering an area of 10 degrees on a side was made in the region of the Lagrange point by scanning in azimuth and allowing the sky to drift through the field of view.

The system was calibrated astronomically by taking scans across the Magellanic clouds and the zodiacal light at several elongations. It was also calibrated absolutely in the laboratory using a standard tungsten filament lamp. The Lagrange point scans are being reduced by averaging the ordinates on the recorder chart for 1 degree square of sky area. The mean intensity of each square and the standard deviation from this mean are computed, excluding squares containing bright sters.

Preliminary reductions show no indication of the presence of a dust cloud. It is hoped, with further data reduction, to place an upper limit on the possible dust cloud brightness corresponding to the deviations from the night sky brightness. The particle density corresponding to this brightness will be calculated.

3

References

- Kordylewski, K., 1961a, Libration clouds in the Earth-Moon system:

 Internat. Astron. Union Circ. no. 1760, p. 1.
- Kordylewski, K., 1961b, Libration clouds in the Earth-Moon system: Internat. Astron. Union Circ. no. 1779, p. 1.
- Lagrange, J. L., 1776, Oeuvres, v. 4: Akad. Wiss. Berlin Mem., p. 255.
- Morris, E. C., and Stephens, H. G., 1963, Photographic investigations of the Earth-Moon libration regions L₄ and L₅ from Mt. Chacaltaya, Bolivia: U.S. Geol. Survey, Astrogeologic studies annual progress report, August 25, 1961 to August 24, 1962, pt. A, p. 64-67.
- Shoemaker, E. M., 1962, Sampling the Moon through Kordylewski's clouds [abs.]: Jour. Geophys. Research, v. 67, no. 4, p. 1656-1657.



SEMI-MICRO X-RAY FLUORESCENCE ANALYSIS OF TEXTITES USING

50 MILLIGRAM SAMPLES

200

by Harry J. Rose, Jr., Frank Cuttitta,

Maxwell K. Carron, and Robena Brown

Introduction

X-ray fluorescence spectroscopy has been applied to the determination of the major constituents in materials of geologic interest (Rose et al, 1962; Flanagan et al, in press) using relatively large amounts of sample. This technique has been adopted to permit the semi-micro analysis of rare specimens where only very small quantities (< 100 mg) of material are available. The analysis of the light elements has been made possible by advances both in the technology of instrumentation and in techniques of sample preparation. It is well known that the intensity of the fluorescent: radiation decreases sharply with a decrease in the atomic number (Z) of the element being analyzed. This decrease is caused by several factors including diminished fluorescence yield and absorption by air, by the sample, by the diffracting crystal, and by the window of the detector. Moreover, as the radiation becomes softer with decreasing atomic number, the depth from which the excited radiation emerges becomes shallower and shallower. Thus the effective radiation involves only those atoms at or near the surface of the sample, a situation that demands precise and representation sample preparation.

The elimination of air from the spectrometer, by either evacuation of the chamber or by flushing the chamber with helium, is the first step

in increasing the intensity of radiation at the detector. The use of supported thin film windows (Balis et al, 1962) on the detectors results in higher intensities by reducing absorption by the window and extends the useful range of the technique to wavelengths beyond 10 angstroms.

Accurate quantitative determination of the light elements depends primarily on sample preparation and particularly on the surface of the specimen submitted to the X-ray beam. As mentioned above, the particles at or near the surface provide the effective signal for analysis. The point beyond which no increase in signal can be observed regardless of increase in sample thickness (infinite depth) is reached for CaO in less than 100 microns and for MgO in less than 50 microns. It is evident, therefore, that the surface of the prepared specimen must be homogeneous and a true representation of the sample.

Fusion of the sample in Li₂B₄O₇ eliminates many of the problems inherent in the X-ray fluorescence analysis of powdered samples (Andermann, 1961; Rose et al, 1962) such as the effects of particle size and crystal structure. The addition of a strongly absorbing element, such as lanthanum, minimizes absorption differences among samples resulting from variations in matrix and thus obviates the need for absorption corrections or for standards matching the composition of the material under study.

The method described initially (Rose et al., 1962) required a 250 mg sample. Although this amount is considerably less than the quantity used for routine chemical analysis, there are instances when

smaller quantities must be analyzed. The effort here was directed towards reducing the sample size to 50 mg by determining the minimum layer
of fused sample necessary to maintain the desired signal for the elements
being analyzed.

X-ray fluorescence method

The fusion mixture consists of 50 mg of sample, 50 mg La203, and 340 mg Li₂B₄O₇. The components are mixed in a boron carbide mortar, transferred to a graphite crucible with a cone-shaped internal base, and fused at 1100°C for 10 minutes. The bead is allowed to cool in the graphite crucible. Cooling may be accomplished more rapidly by placing the crucible on a large copper plate which dissipates the heat more readily. Sufficient boric acid is weighed out to bring the weight to 460 mg. The glass bead is then ground. The grinding vial consists of a lucite cylinder provided with two caps containing tungsten carbide inserts for covering both ends of the cylinder. The bead, which must be crushed before grinding, is placed cone-side-up in the grinding vial with one of the caps and insert in place. A 1/2-inch drive pin punch is placed down the cylinder on top of the bead and is then tapped with a hammer. The weighed boric acid is added to the vial along with a 1/4inch tungsten carbide ball and the upper cap placed on the cylinder. The sample is then ground on a mixer grinder for 10 minutes, reducing the sample to about 325 mesh. The ground powder is then pressed into a pellet 1 inch in diameter. For additional strength the pellet is prepared as a double layer using boric acid as backing (Rose and Flanagan, 1962). It is essential that the sample layer be spread uniformly on the surface of the boric acid before final pressure is applied. To obtain maximum intensity for Si and Al, pressure in excess of 50,000 psi must be used. The preparation of sample must be done consistently with attention to all details to insure the best results.

A single channel spectrometer was used for this study. The crystals, wavelengths, and detectors are given in table 8.1. Because the fluorescent radiation of elements $Z \leq 22$ is absorbed by air, the spectrometer chamber is flushed with helium for the determination of these elements. It is generally necessary to flush the chamber for about one minute between sample changes to allow the system to come to equilibrium.

Granite G-1, diabase W-1, and a one-to-one mixture of the granite and diabase are used as reference standards. National Bureau of Standards standard samples and other samples analyzed at the U.S. Geological Survey serve as additional reference materials to extend the range of the elements being determined.

Results of X-ray fluorescence and chemical determinations on six samples of Java tektites are compared in table 8.2.

Chemical analytical methods

Six javanites were carefully selected from a collection of about 80 specimens to represent the range of the indices of refraction and specific gravities of the Java tektite collection. The specimens are

Table 8.1 Summary of crystals, detectors and wavelengths

Element	K.A	Crystal	Detector, Counter*	Path
Si	7.125	gypsum	proportional	Не
A1	8.337	gypsum	proportional	Не
Fe	1.936	LiF**	scintillation	Air
Cn	3.358	Eddt	proportional	Не
K	3.741	gypsum	proportional	Не
Mn	2.102	Lif	scintillation	Air
Ti	2.748	Lif	scintillation	He

^{*} Pulse height analysis, channel width 12V, base level 4.5V.

Ethylene diamine ditartrate substituted for gypsum in samples high in K₂O.

^{**} Lithium fluoride.

Comparison of X-ray* and chemical analyses of 6 Java tektites Table 8.2

	JS-12	12	JS-9	6	JS-5	2	JS-6	9	JS-3	æ	JS-11	11
	X-ray	Chem.	X-ray	Chem.	X-ray	Chem.	X-ray	Chem.	X-ray	Chem.	X-ray	Chem.
S10 ₂	74.4	74.2	73.5	73.4	74.2	73.8	74.7	74.4	72.3	72.3	72.5	72.3
A1203	11.6	11.1	11.3	11.4	11.5	11.3	11.3	11.2	11.3	11.3	11.4	11.6
Fe203+	5.70	5.67	5,65	5.63	5.35	5.28	5.66	5.52	6.28	6.14	6.17	6.22
CaO	2.29	2.25	2.70	2.70	2.65	2.75	2.47	2.36	2.97	2.91	2.79	2.87
K20	2,23	2.24	2.27	2.28	2.25	2.25	2.32	2.29	2.22	2.22	2.17	2.15
MnO	0.10	0.11	0.11	0.10	0.10	60.0	0.11	0.10	0.10	0.11	0.11	0.11
T102	0.68	0.67	0.68	0.68	0.66	0.67	0.69	69.0	0.70	0.70	69.0	0.68
ND**	1.	1.5073	H	1.5089	Η.	1.5102	.	1.5112		1.5127	1.	1.5141
Sp.G.**		2.443		2.464	.4	2.439		2.426		2.468		2.48

Total Fe as Fe_2O_3

X-ray determination made on a single pellet.

Index of refraction and specific gravity by Janet Marteka and E. C. T. Chao.

**

listed in table 8.2 in order of increasing index of refraction. The tektites were analyzed for SiO₂, Al₂O₃, total iron as Fe₂O₃, CaO, K₂O, TiO₂, and MnO₂ by gravimetric, spectrophotometric, volumetric, flamephotometric, and spectrographic techniques. The chemical results are averages of duplicate determinations by the various methods. Using these different techniques, the chemical determinations were closely monitored by similar determinations on granite G-1, diabase W-1, and selected National Bureau of Standards certified samples.

Silica was determined spectrophotometrically using a molybdenum blue method (Bunting, 1944), gravimetrically by a volatilization-formaldehyde method described by Carron and Cuttitta (1962), and also by a combined gravimetric and photometric procedure (Jeffery and Wilson, 1960). Alumina (A1203) was determined by measuring the absorbance of the calcium aluminum alizarin red-S complex in a weakly acidic medium (pH 4.5) at 485 mµ (Parker and Goddard, 1950). Interference from iron was eliminated by use of potassium ferricyanide and thioglycolic acid as complexing agents.

Total iron was determined spectrophotometrically with omphenanthroline (Cuttitta, 1952 and Sandell, 1959) and by a magnetic susceptibility method developed by Thorpe, Senftle, and Cuttitta (1963). Calcium oxide was determined by flamephotometry (Kramer, 1957), and by a semi-micro, autematic, photometric titration with EDTA in the pH range 12.1-12.3 at 590 mmu using murexide as the indicator. Potassium oxide was determined flame-photometrically at 766 mmu using an instrument with a photomultiplier attachment. The sample was analyzed by bracketing between the closest potassium standards (Ray, 1956; Willgallis, 1957; Voinovitch and Debras,

1958). Titanium was determined spectrophotometrically with disodium-1, 2 - dihydroxybenzene - 3, 5 - disulfonate (tiron) (Yoe and Armstrong, 1947). The interference of iron was overcome by reduction with ascorbic acid at pH 4.7. The purple permanganate color was utilized for the spectrophotometric determination of manganese. The oxidation was effected with ammonium persulfate (peroxysulfate) at the boiling point in a phosphoric-nitric medium in the presence of silver nitrate. Manganese was also determined by Janet D. Fletcher using a quantitative spectrographic method similar to that described by Bastron, Barnett, and Murata (1960).

References

- Andermann, George, 1961, Improvements in the X-ray emission analysis of cement raw mix: Anal. Chemistry, v. 33, p. 1689-1694.
- Balis, E. W., Bronk, L. B., Pfeiffer, H. G., Welbon, W. W., Winslow,
 E. H., and Zemany, P. D., 1962, Improved components for the X=ray
 emission analysis of the light elements: Anal. Chemistry, v. 34,
 p. 1731-1733.
- Bastron, Harry, Barnett, P. R., and Murata, K. J., 1960, Method for the quantitative spectrochemical analysis of rocks, minerals, ores, and other materials by a powder D=C arc technique: U.S. Geol. Survey Bull. 1084-G, p. 165-182.
- Bunting, W. E., 1944, The determination of soluble silica in very low concentration: Indus. Eng. Chemistry, Anal. Ed., v. 16, p. 612-615.

References--Continued

- Carron, M. K., and Cuttitta, Frank, 1962, Determination of silica in tektites and similar glasses by volatilization: Art. 30 in U.S. Geol. Survey Prof. Paper 450-B, p. B78-B79.
- Cuttitta, Frank, 1952, The colorimetric determination of total iron with o-phenanthroline--A spectrophotometric study: U.S. Geol. Survey TEI-223, 25 p.
- Flanagan, F. J., Rose, H. J., Jr., Cuttitta, Frank, and Carron, M. K., in press, Assessing the accuracy of the analysis of tektites by the X-ray quantometer: U.S. Geol. Survey Prof. paper.
- Jeffery, P. G., and Wilson, A. D., 1960, A combined gravimetric and photometric procedure for determining silica in silicate rocks and minerals: The Analyst, v. 85, p. 478-486.
- Kramer, Henry, 1957, Flame photometric determination of calcium in phosphate, carbonate, and silicate rocks: Anal. Chim. Acta, v. 17, p. 521-525.
- Parker, C. A., and Goddard, A. P., 1950, The reaction of aluminum ions with alizarin-3-sulphonate, with particular reference to the effect of addition of calcium ions: Anal. Chim. Acta, v. 4, p. 517-535.
- Roy, Norman, 1956, Flame photometric determination of sodium, potassium, calcium, magnesium, and manganese in glass and raw materials:

 Anal. Chemistry, v. 28, p. 34-39.
- Rose, H. J., Jr., Adler, Isidore, and Flanagan, F. J., 1962, Use of La₂O₃ as a heavy absorber in the X-ray fluorescence analysis of silicate rocks: Art. 31 in U.S. Geol. Survey Prof. Paper 450-B, p. B80-B82.

References--Continued

- Rose, H. J., Jr., and Flanagan, F. J., 1962, X-ray fluorescence determination of thallium in manganese ores: Art. 32 in U.S. Geol.

 Survey Prof. Paper 450-B, p. B82-B83.
- Sandell, E. B., 1959, Colorimetric determination of traces of metals, 34 ed.: New York, Interscience, p. 537-542.
- Shapiro, Leonard, and Brannock, W. W., 1962, Rapid analysis of silicate, carbonate, and phosphate rocks: U.S. Geol. Survey Bull. 1144-A, p. 1-56.
- Thorpe, A. N., Senftle, F. E., and Cuttitta, Frank, 1963, Magnetic and chemical investigations of iron in tektites: Nature, v. 197,
- Voinovitch, I. A., and Debras, J., 1958, Determination of sodium, potassium, and lithium in silicates by flame photometry: Indus. Ceramique, no. 502, p. 321-327.
- Willgallis, A., 1957, Flame photometric determination of alkali metals in rocks: Zeitschr. Anal. Chemie, v. 157, p. 249-257.
- Yoe, J. H., and Armstrong, A. R., 1947, Colorimetric determination of titanium with disodium-1, 2-dihydroxybenzene-3, 5-disulfonate:

 Anal. Chemistry, v. 19, p. 100-102.



COMPUTER ANALYSIS OF AREAL MICROPHOTOMETER DATA

FROM LUNAR PHOTOGRAPHS

by A. T. Miesch and C. W. Davis

A computer program for analysis of microphotometer data has been partially completed since the last report period. As described previously (Davis and others, 1963), the program is designed to provide a group of statistics regarded as potentially useful in geologic studies of the lunar surface. In a preliminary study, some of the statistics have been computed using stock programs already available in the Geological Survey program library, but the volume of this work has been small because of present limitation on data generation and preparation. A machine-automated system of data generation and preparation is being developed. In addition to preliminary computation of some of the statistics to be provided by the program being prepared, the experiments of Henderson and Fischer (1963) with autocorrelation, have been extended to two dimensions.

The techniques used and results from the preliminary computations are given in the present report.

Microphotometer measurements were taken on a full-moon photographic plate (scale 1:2,000,000) within a rectangular area in the vicinity of Milichius and Milichius A, between Kepler and Copernicus (fig. 9.1).

^{1/} Branch of Geochemical Census, U.S. Geological Survey

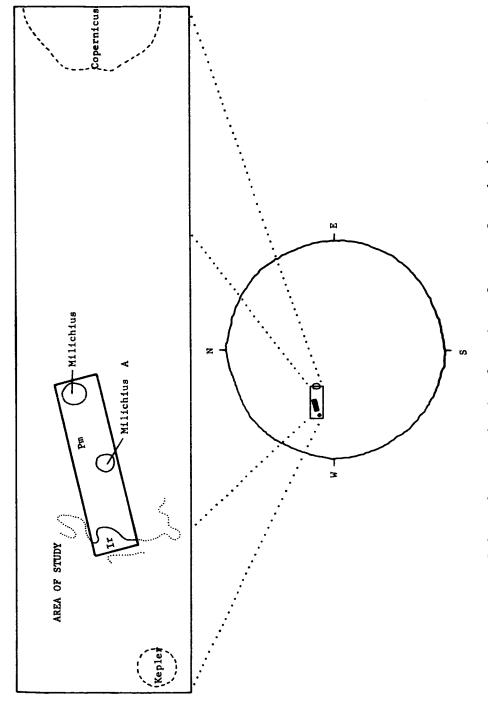


Figure 9.1 Index map showing location of area of study (Ir, Apenninian regional material; Pm, Procellarian mare material).

A geologic map that includes this area has been published (Hackman, 1962). The measurements, of 0.1 millimeter square areas on the photographic plate, were taken along traverses spaced one millimeter apart; spacing of measurements within traverses were also at one millimeter (15 traverses, 60 readings per traverse). This 15.5 x 65 millimeter area on the plate is equivalent to a 31 x 130 kilometer area on the Moon, with measurements representing 0.2 x 0.2 kilometer squares spaced 2 kilometers apart. The measurements are in the range 0 to 10,000, and are proportional to transmission of the lunar plate; for the present discussion the measurements will be regarded as direct measurements of albedo.

Of the several geologic units present in this area, those studied were the large areas of Procellarian mare material and Apenninian regional material. The areas of crater rim, slope, and floor material at Milichius and Milichius A were not examined. More detailed microphotometer scanning will be required for such small areas.

A highly generalized flow chart for the computer program being prepared is given in figure 2. Parts A and D of the program are completed, and parts B and C are nearing completion. The present report concerns preliminary experiments in the application of some statistics that will be provided by parts A, D, E, and F.

In part D the mean, standard deviation, skewness, and kurtosis are computed from formulae for Fisher's K-statistics, as given by Bennett and Franklin (1954, p. 81-82). In current work, however, the skewness and kurtosis have been computed from equivalent formulae for grouped data.

Estimation of trends (part E) and determination of trend deviations (part F) is done in order to separate regional and local components of lunar albedo variation patterns. The philosophy of the approach used, as viewed in stratigraphic studies, was first stated by Krumbein (1956) and a description of the general computational procedure followed is presented by the same writer elsewhere (Krumbein, 1959). Trend analysis, as the method is commonly termed, consists of fitting a polynomial function of order n to data collected over a map area. Least square techniques of multiple regression are employed, using X and Y geographic coordinates as independent variables. The fitted function has the form:

$$A_{c} = b_{o} + b_{1}X + b_{2}Y + b_{3}X^{2} + b_{4}XY + b_{5}Y^{2} + b_{6}X^{3} ... b_{1}Y^{n}.$$
 (1)

The order, n, of the polynomial function used to describe the trend can be chosen, in some cases, from prior knowledge of the causes underlying the trend, or may be chosen using various statistical criteria. When the b-coefficients have been estimated, the computed value of albedo, A_c , is easily determined for any point (X,Y) within the area of study. The trend equation (1) is an estimate of a function that describes the variation in albedo attributable to factors and processes that acted across the entire area of study in a more or less continuous manner. The deviation of measured or observed values of albedo, A_c , from the trend values, A_c , may reflect, in part, the presence of local factors and processes

that have affected the albedo. A trend deviation, A_r , is given by:

$$A_{r} = A_{o} - A_{c}$$
 (2)

Some part of the deviation of observed measurements from the computed trend is a result of measurement error and of error in the estimation of the trend (e.g., error in estimates of the b-coefficients, or use of an improper type of function).

Statistical criteria used to select the order, n, of the polynomial function are as follows: (1) analysis of variance, (2) cumulative percent sums of squares accounted for by successive orders of polynomial functions, and (3) an autocorrelation technique. The analysis of variance technique applied to polynomial multiple regression is given by Bennett and Franklin (1954, p. 429-436). Results of the analyses, applied to the various polynomial models used in studying the mare material and regional material, are given in tables 9.1 & 9.2, respectively. The cumulative sums of squares are also given in tables 9.1 & 9.2. The analyses of variance indicate that first, second, and third order polynomial surfaces (functions with two independent variables, X and Y geographic coordinates) account for statistically significant portions of the total variance of albedo in both areas studied; the fourth order surface is significant in the case of Procellarian mare material. However, in both cases (tables 9.1 and 9.2) the proportion of the total sum of squares accounted for by surfaces beyond the second order is small.

Procellarian mare material: Analysis of variance of polynomial regression surfaces Table 9.1

					Propesum of store tor thighe	Proportion of total sum of squares accounted for by successively higher order terms
Source	Sum of squares	freedom	Mean square	ŢŦ	ercent	Cumulative percent
First order terms Deviations from 1st order	15278×10 ⁴ 37345×10 ⁶	2 630	7639×10 ⁴ 59×10 ⁴	1291/	29.0	29,0
Second order terms Deviations from 2nd order	6599x10° 30746x10°	3 627	2200×10* 49×10*	451/	12,5	41,5
Third order terms Deviations from 3rd order	1352×10 ⁴ 29394×10 ⁴	4 623	338×10 ⁴ 47×10 ⁴	$7\sqrt{1}$	2,6	44,1
Fourth order terms Deviations from 4th order	1771×10° 27623×10°	5 618	354x10 ⁴ 45x10 ⁴	8 ₁ /	3.4	47.5

 $\frac{1}{2}$ Significant at greater than 0.99 probability level.

Table 9.2. Apenninian regional material: Analysis of variance of polynomial regression surfaces

			40			Pro sum of for hig	Proportion of total sum of squares accounted for by successively higher order terms
3927x10 ⁴ 2 22714x10 ⁴ 88 8134x10 ⁴ 3 14530x10 ⁴ 85 2366x10 ⁴ 4 12164x10 ⁴ 81 1491x10 ⁴ 5 10673x10 ⁴ 5 10673x10 ⁴ 6 9876x10 ⁴ 6		f squares	regrees or freedom	Mean square	দি	Percent	Percent Cumulative percent
22714x10 ⁴ 88 8184x10 ⁴ 3 14530x10 ⁴ 85 2366x10 ⁴ 4 12164x10 ⁴ 81 1491x10 ⁴ 5 10673x10 ⁴ 5 9876x10 ⁴ 6		27x10 ⁴	2	1964×104	7.611/	14.7	14.7
\$\cdot 81\boldsymbol{3}(4) \tag{4} \tag{5}30\times 10^4 \tag{8} \tag{5} \tag{4} \tag{2}36\times 10^4 \tag{4} \tag{4} \tag{1}2164\times 10^4 \tag{8} \tag{8}1 \tag{1}491\times 10^4 \tag{5} \tag{1}0673\times 10^4 \tag{5} \tag{6} \tag{9}876\times 10^4 \tag{6} \tag{6}		14×104	88	258×10*			
14530x10° 85 2366x10° 4 12164x10° 81 1491x10° 5 10673x10° 5 76 9876x10° 6	.	84×104	က		15.95^{1}	30.7	45.4
2366x10 ⁴ 4 rd order 12164x10 ⁴ 81 s 1491x10 ⁴ 5 th order 10673x10 ⁴ 76 th order 9876x10 ⁴ 6		30x10*	85	171×10*			
12164x10 ⁴ 81 1491x10 ⁴ 5 10673x10 ⁴ 76 797x10 ⁴ 6		66×104	7	592×104	3.951/	8.9	54.3
1491×10 ⁴ 5 10673×10 ⁴ 76 797×10 ⁴ 6 9876×10 ⁴ 70		64×104	81	150×10 ⁴			
10673×10 ⁴ 76 797×10 ⁴ 6		91x104	5	298×10 ⁴	2.13	5.6	59.9
797 x 10 ⁴ 6 9876 x 10 ⁴ 70		73×10 ⁴	92	140×10 ⁴			
9876×10 ⁴ 70	. <u>u</u> u 11 î	97×10 ⁴	9	133×10*	0.94	3.0	62.9
		76×10 ⁴	70	141×10 ⁴			
	•						

 $\frac{1}{2}$ / Significant at greater than 0.99 probability level.

The suitability of the second order surfaces for describing the trends is further evidenced by application of the autocorrelation technique applied to the regression or trend deviations. The autocorrelations of deviations from trends beyond the second order approach zero or are negative in one case and appear to approach stable values \frac{1}{2} in the other (fig. 9.3). It appears, therefore, that the second order trends are the lowest order polynomial functions having deviations which are not autocorrelated. A previous application of this technique is given by Connor and Miesch (1964).

Experiments with autocorrelation of microphotometer data from lunar photographs were begun by Henderson and Fischer (1963, p. 54-56). The same technique they used has now been applied to data collected over an area, rather than along a single trace, to provide "serial correlation" surfaces. The autocorrelation curves obtained by Henderson and Fischer, and the serial correlation surfaces from current work, serve several

^{1/} The stable values (figure 9.3, Procellarian mare) are approximately 0.55 and 0.35, but statistical theory for assessing the significance of these two-dimensional autocorrelation coefficients is not available. They are tentatively regarded as non-significant because they are not greatly less than those obtained with deviations from two preceding lower order trends. However, trends of higher than fourth order are currently being estimated so that the autocorrelations of deviations from the higher order trends may be examined.

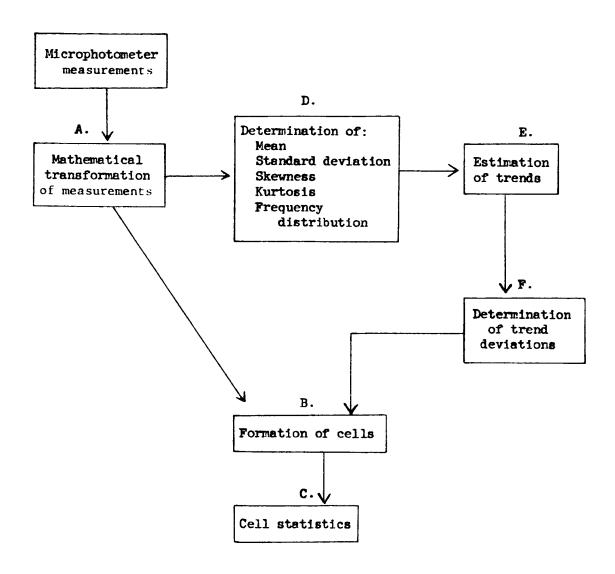


Figure 9.2 Generalized flow chart for computer program being prepared to analyze microphotometer data (Davis and others, 1963).

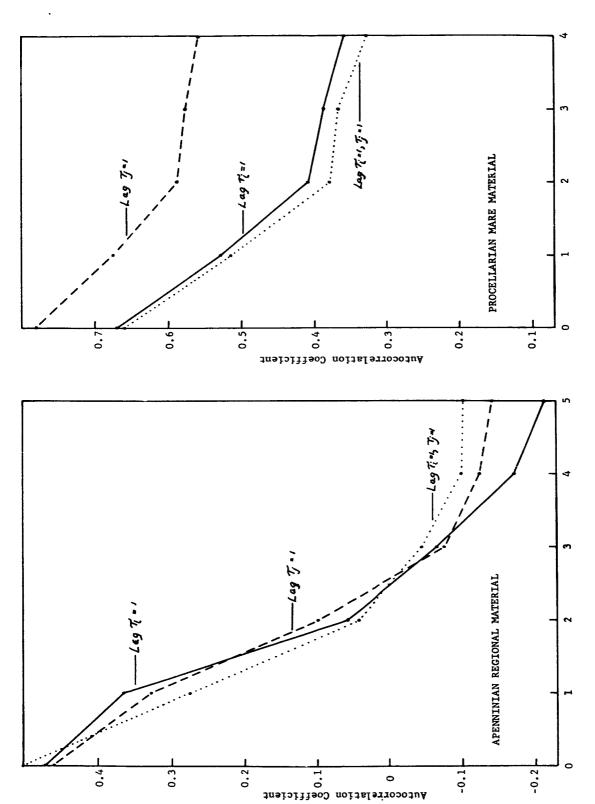


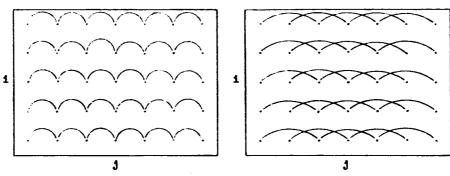
Figure 9.3. Autocorrelation curves computed from original data (order of trend = 0) and deviations from trends of order 1 to 5 i is lag in j direction (Apenninian regional material) and 1 to 4 (Procellarian mare material). 1 is lag in i direction; (see figures 9.7 and 9.13). material).

purposes: (1) to determine characteristic parameters of various geologic units empirically, as a rock correlation tool, (2) to determine optimum spacing of microphotometer readings for finding gross photometric properties in future work, and (3) as a measure of fineness or coarseness of albedo texture patterns exhibited by the areas examined.

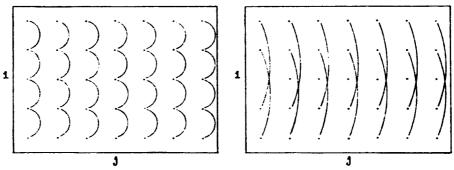
The basic principles of the autocorrelation method are given by Henderson and Fischer (1963). Blackman and Tukey (1958) present the theory and application in detail. A previous application to two-dimensional (map) data is described by Horton and others (1962), who proceed a step farther than we do here to the determination of the power spectrum. The serial correlation surfaces were obtained by lagging areal data in two dimensions (figs. 9.4a, 9.4b, and 9.4c). Viewing each row and column of data points on the serial correlation surface as a trace or "series," and following the terminology of Ezekiel and Fox (1959, p. 337), the surfaces may be viewed as containing both cross and serial correlations; cross sections of the surfaces are analogous to autocorrelation and serial correlation curves (fig. 9.5).

Procellarian mare material

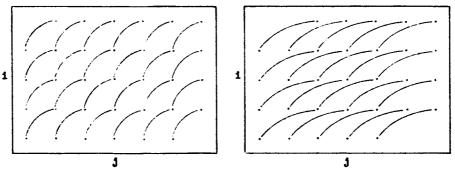
Statistical results computed from the frequency distribution of microphotometric measurements on Procellarian mare material (fig. 9.6a) are as follows:



A. Pairing of data points with lags $\mathcal{T}_{j} = 1$ and $\mathcal{T}_{j} = 2$. Curved lines connect data pairs. Correlation coefficients appear at points a and b on the serial correlation surface (fig. 5).

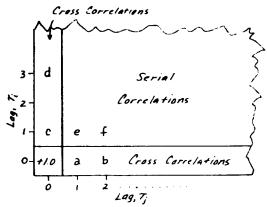


B. Pairing of data points with lags $\mathcal{T}_1 = 1$ and $\mathcal{T}_1 = 3$. Curved lines connect data pairs. Correlation coefficients appear at points c and d on the serial correlation surface (fig. 5).

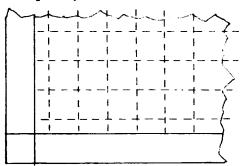


C. Pairing of data points with lags $\mathcal{T}_1 = 1$, $\mathcal{T}_3 = 1$ and $\mathcal{T}_1 = 1$, $\mathcal{T}_3 = 2$. Curved lines connect data pairs. Correlation coefficients appear at points e and f on the serial correlation surface (fig. 5).

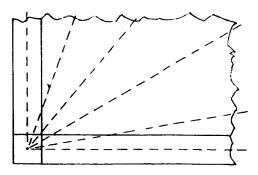
Figure 9.4. Method of lagging areal data for construction of serial correlation surfaces.



A. Locations of serial and cross correlations (between rows and columns of data points) on the serial correlation surface

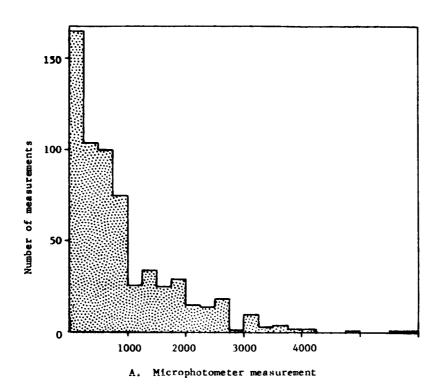


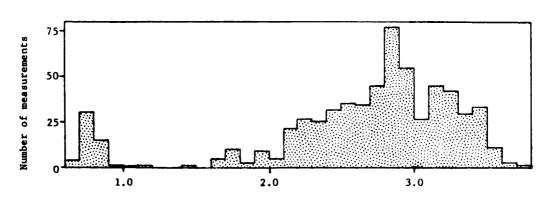
B. Each cross section of the serial correlation surface that parallels a boundary of the surface (dashed lines) is a composite serial correlation curve for a group of trace pairs



C. Each cross section of the serial correlation surface that passes through lag 0,0 (dashed lines) is a composite autocorrelation curve for a group of traces parallel to and lagged in the direction of the cross section

Figure 9.5. Component parts of the serial correlation surface.





B. Log microphotometer measurement

Figure 9.6. Histograms of microphotometer measurements: Procellarian mare material.

Number of measurements ----- 633

Arithmetic mean------ 902

Standard deviation----- 912

Skewness----- 1.71²/

Kurtosis----- 3.51²/

Chi square----- 163²/ (degrees of freedom = 10)

Estimates of skewness and kurtosis, along with the high value of chi square, indicate that the measurements made on Procellarian mare material in this region are not normally distributed; the confidence interval for the arithmetic mean, therefore, cannot be estimated accurately. The data are, in fact, positively skewed to a marked degree.

On log transformation of the data (fig. 9.6b), the general form of the frequency distribution resembles a normal curve, but a secondary mode containing about 9 percent of the distribution occurs at the low values. The gap between the two modes is sufficiently prominent to use in making an objective separation of the measurements into two classes. Assuming that the secondary mode has not been caused by photographic or instrumental error, this implies that two distinct and easily separable kinds

^{2/} These estimates are considerably beyond the range of estimates to be expected (0.99 probability) with data drawn from a normally distributed population. In specifying the degrees of freedom available for the test no account was given to the serial correlation in the data displayed on figure 9.10.

of geologic material are present in the area previously mapped as mare. Most of the low measurements represent an area west of Milichius A; a few form a cluster east of Milichius A and several are from scattered locations on figure 9.7.

A number of interpretations could be advanced to account for the two distinct types of geologic materials within the mare. A preferred interpretation explains the two materials as (1) rays and other ejecta with varying degrees of albedo superimposed on the mare, and (2) barren or uncovered mare with distinctly lower albedo. The interpretation follows, then, that only 9 percent of the mare is barren of ray and other ejecta materials.

Additional evidence for the dominant influence of ray material on the albedo of mare areas is gained through trend analysis, wherein fitted regression surfaces appear to reflect the occurrence of craters and ejecta material within and adjacent to the area studied. The fitted first order trend (fig. 9.8) slopes to the west, displaying a general increase in albedo toward Milichius, the larger of the two craters in the area studied. The second order trend (fig. 9.8) shows a general low albedo about midway between Milichius A and the Apenninian regional material west of the area studied. Contours of deviations of microphotometer measurements from the computed second order trend (fig. 9.9) are thought to show local accumulations of brighter ray material within the area, in contrast to the trend which shows the regional distribution. The local accumulations occur mainly around the Milichius and Milichius A craters

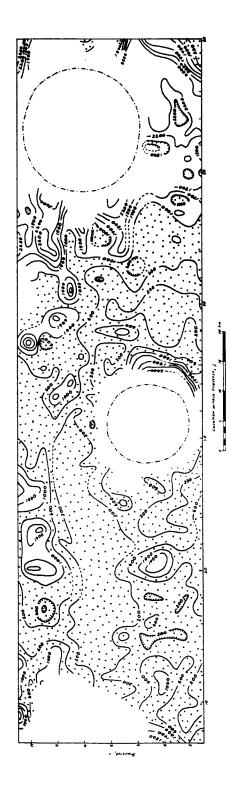


Figure 9.7. Contour map of original microphotometer measurements: Procellarian mare material. Areas of less than average brightness shown by stipple pattern.

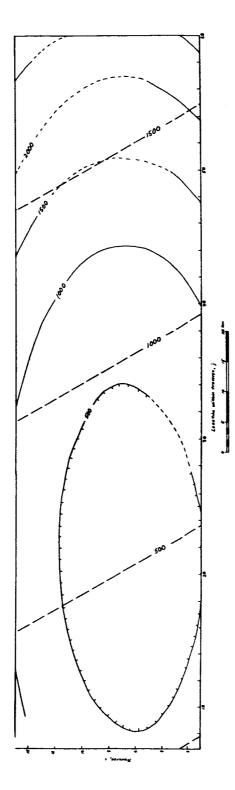


Figure 9.8. Contour map of first order (dashed lines) and second order (solid lines) polynomial surfaces (trends) fitted to microphotometer data in figure 9.7: Procellarian mare material.

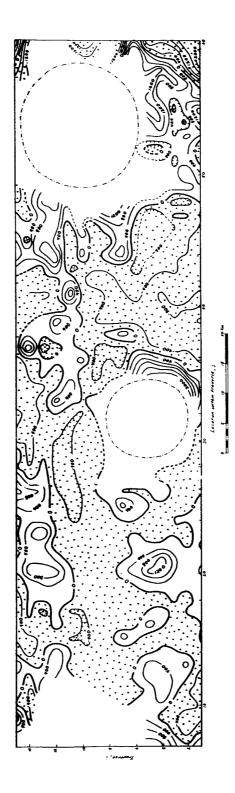


Figure 9.9. Contour map of deviations of original microphotometer measurements from fitted second order trend: Procellarian mare material. Areas of negative deviations shown by stipple pattern.

and adjacent to the Apenninian regional material in the western portion of the area studied.

The serial correlation surface shown in figure 9.10 indicates that microphotometer readings might have been spaced several millimeters apart without significant loss of information. Certainly, it appears that spacing closer than one millimeter would result in redundancy of measurement and loss of efficiency. Some additional work will be necessary to determine whether this conclusion can be extended to other mare areas. The optimum sampling spacing, of course, depends on the coarseness of the reflectivity texture pattern, and the texture of the mare area appears to be coarser than that of the ejecta blanket to the west (fig. 9.16). This could also be inferred from the nature of the rock types thought to be present in the two areas, volcanic flows in the mare area covered by widely distributed ray material, and crushed rock and great blocks of ejecta blanket (Hackman, 1962). The autocorrelation curves in figure 9.11 which are radial cross sections of the serial correlation surface, demonstrate the variation of such curves with direction. The curves obtained by Hendersom and Fischer (1963, p. 56) for single microphotometer traces across Procellarian mare areas are shown on the same figure. The apparent difference between the autocorrelation curves obtained in the earlier work and those resulting from the present work probably results largely from the manner in which the two sets of data were obtained. and Fischer used an average measurement over contiguous one millimeter intervals, whereas in the present work measurements were taken over small

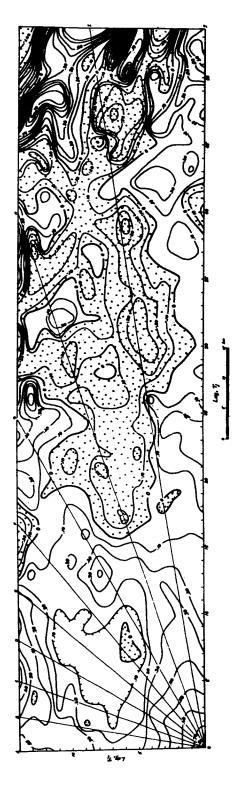


Figure 9.10. Contour map of serial correlation surface: Procellarian mare material. Negative areas of the surface are shown by stipple pattern. Radial lines show locations of cross sections given in figure 9.11.

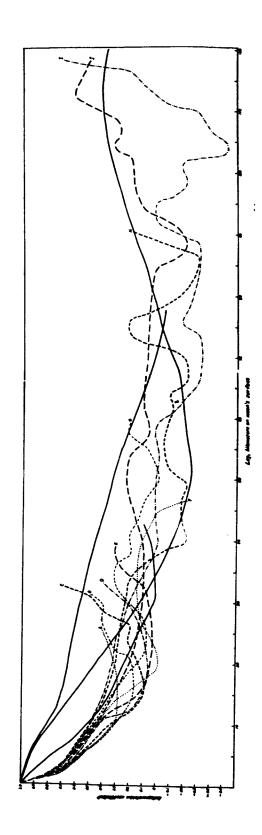


Figure 9.11. Autocorrelation curves for Procellarian mare material. Dashed and dotted curves are cross-sections of figure 9.10 which pass through point for lag 0, 0. Solid lines are curves from adjusted to a comparable scale. Henderson and Fischer (1963)

discontinuous areas. The progressively higher values of the autocorrelation curves, for small lags, from north-south traces to east-west traces (fig. 9.11) reflects an east-west grain in the albedo texture pattern (fig. 9.7). Whether or not autocorrelation curves or serial correlation surfaces will be useful in the identification of rock types cannot be determined until the calculations have been applied more extensively.

Apenninian regional material

Statistical results computed from the frequency distribution of microphotometer readings in Appeninian regional material (fig. 9.12) are as follows:

Number of readings----- 91

Arithmetic mean and 0.95

confidence interval---- 3065 ± 359

Standard deviation---- 1720

Skewness----- 0.42

Chi square----- 7.32 (degrees of freedom = 7).

The values of skewness, kurtosis, and chi square are less than the critical values (0.95 probability level) required to reject the hypothesis that the data are normally distributed. The mean albedo is more than three times that of Procellarian mare material and the variation (indicated by the standard deviation) is also considerably higher.

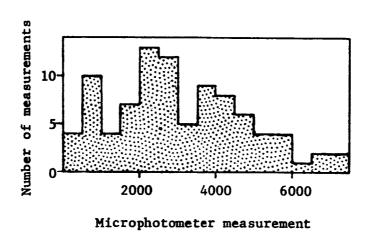


Figure 9.12. Histogram of microphotometer measurements: Apenninian regional material.

A contour map of the microphotometer measurements from the regional material is given in figure 9.13. A second order polynomial surface fitted to the same data shows a significant decrease in brightness toward the blanket margins (fig. 9.14). Similarly, contours on deviations of observed data from the computed trend (fig. 9.15) appear to reflect concentrations of darker material in the marginal areas. Hackman (1962) has interpreted the ejecta blanket in this area to be thin along its margins; in places it is interpreted to be so thin that broad areas of underlying material are exposed within its mapped boundaries.

The serial correlation surface shown in figure 9.16 indicates that the texture of the albedo pattern on the ejecta blanket is finer than that of the Procellarian mare. It indicates further that some loss of information may occur in spacing readings one millimeter apart. In future microphotometer analysis of ejecta blanket material the spacing of readings should be reduced to some smaller interval. No conclusion can be drawn, as yet, as to whether the nature of the serial correlation surface is characteristic of areas covered by Apenninian regional material.

Conclusions

Statistical analysis of microphotometer data, employing techniques to be made more readily available through the program being prepared (Davis and others, 1963) and through full automation of the instrument, yields information that can be interpreted in terms of known geologic features of the lunar surface. Measures of overall albedo, variation in

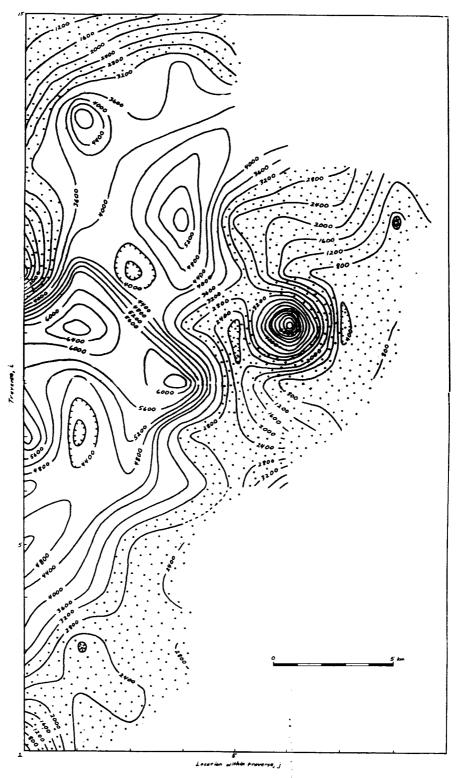


Figure 9.13. Contour map of original microphotometer measurements: Apenninian regional material. Areas of less than average brightness shown by stipple pattern.

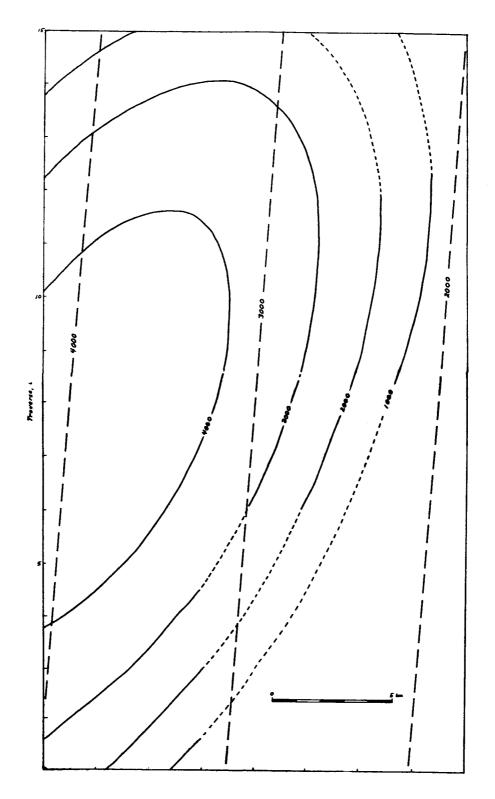


Figure 9.14. Contour map of first order (dashed lines) and second order (solid lines) polynomial surfaces (trends) fitted to microphotometer data in figure 9.13: Apenninian regional material.

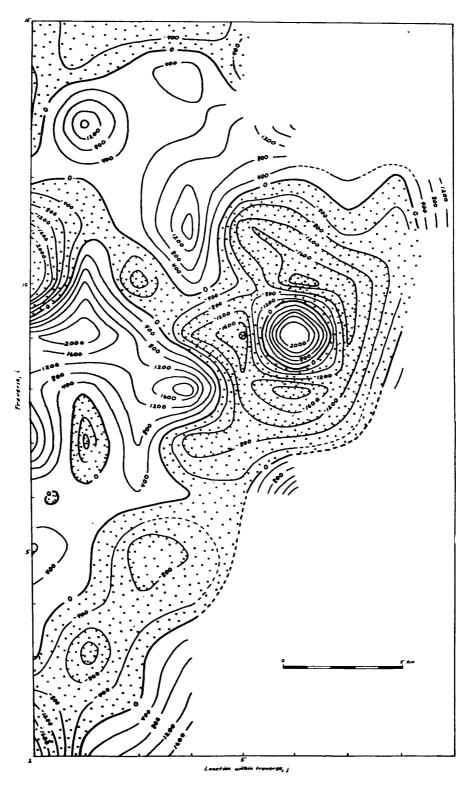


Figure 9.15. Contour map of deviations of original microphotometer measurements from fitted second order trend: Apenninian regional material. Areas of negative deviations shown by stipple pattern.

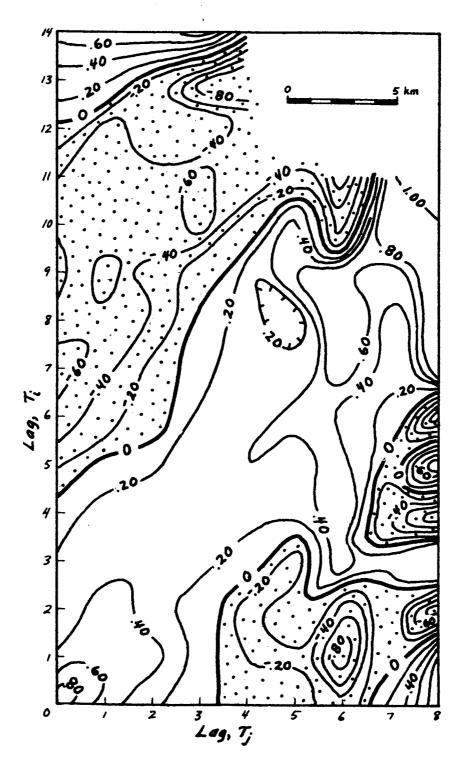


Figure 9.16. Contour map of serial correlation surface: Apenninian regional material. Negative areas of the surface are shown by stipple pattern.

albedo, textural properties of albedo patterns, and regional gradation in albedo are provided, as well as estimates of their statistical significance. The statistical data may serve to quantify observations made during the course of lunar mapping on photographs, to test the accuracy of certain observations, to extract subtle but geologically meaningful features of mapped rock units, and eventually to identify and correlate rock units.

References

- Bennett, C. A., and Franklin, N. L., 1954, Statistical analysis in chemistry and the chemical industry: New York, John Wiley and Sons, 724 p.
- Blackman, R. B., and Tukey, J. W., 1958, The measurement of power spectra:

 New York, Dover Publications, 190 p.
- Connor, J. J., and Miesch, A. T., 1964, Application of trend analysis

 to geochemical prospecting data from Beaver County, Utah, in

 Transactions, Symposium on computers in the mineral industries,

 June 1963: Stanford Univ. Pub. Geol. Sci., v. 9, no. 1, p. 110-125.
- Davis, C. W., Miesch, A. T., Eicher, R. N., and Morris, E. C., 1963,

 Computer analysis of microphotometer data from lunar photographs:

 U.S. Geol. Survey, Astrogeologic studies annual progress report

 August 25, 1961 to August 24, 1962, pt. A, p. 32-50.
- Ezekiel, Mordecai, and Fox, Karl A., 1959, Methods of correlation and regression analysis, 5th ed.: New York, John Wiley and Sons, 548 p.

References--Continued

- Hackman, R. J., 1962, Geologic map and sections of the Kepler region of the Moon: U.S. Geol. Survey Inv. Map I-355.
- Henderson, R. G., and Fischer, W. A., 1963, Applications of analytical methods to a single microdensitometer trace: U.S. Geol. Survey, Astrogeologic studies annual progress report, August 25, 1961 to August 24, 1962, pt. A, p. 51-57.
- Horton, C. W., Hoffman, A. A. J., and Hempkins, W. B., 1962, Mathematical analysis of the microstructure of an area of the bottom of Lake Travis: Texas Jour. Sci., v. 14, p. 131-139.
- Krumbein, W. C., 1956, Regional and local components in facies maps:

 Am. Assoc. Petroleum Geologists Bull., v. 40, no. 9, p. 2162-2194.
- Krumbein, W. C., 1959, Trend surface analysis of contour-type maps with irregular control-point spacing: Jour. Geophys, Research, v. 64, no. 7, p. 823-834.